8-2011

The Effects of Varying Physical Parameterizations and Initial Conditions on Tracer Transport in the National Aeronautics and Space Administration's Goddard Earth Observation System Model, Version 5

Melissa Ree Allen
mallen24@utk.edu

To the Graduate Council:

I am submitting herewith a thesis written by Melissa Ree Allen entitled "The Effects of Varying Physical Parameterizations and Initial Conditions on Tracer Transport in the National Aeronautics and Space Administration's Goddard Earth Observation System Model, Version 5." I have examined the final electronic copy of this thesis for form and content and recommend that it be accepted in partial fulfillment of the requirements for the degree of Master of Science, with a major in Environmental Engineering.

Joshua S. Fu, Major Professor

We have read this thesis and recommend its acceptance:

John B. Drake, Glen A. Tootle, David J. Erickson

Accepted for the Council:
Dixie L. Thompson

Vice Provost and Dean of the Graduate School

(Original signatures are on file with official student records.)

The Effects of Varying Physical Parameterizations and Initial Conditions on Tracer Transport in the National Aeronautics and Space Administration's Goddard Earth Observation System Model, Version 5

A Thesis Presented for the
Master of Science
Degree
The University of Tennessee, Knoxville

Melissa Ree Allen
August 2011

ACKNOWLEDGMENTS

I gratefully acknowledge the valuable instruction, encouragement and advocacy of my advisor and mentor, Dr. Joshua Fu, and his guidance throughout the Environmental Engineering Master of Science degree at the University of Tennessee.

I also thank Dr. John Drake, whose plainspoken but thorough explanation of atmospheric circulation and climate modeling, along with his availability for discussion of such matters, has deepened my understanding and clarified my methods; and Dr. Glenn Tootle, whose teaching, both directly and indirectly inspires excellence.

Additionally, I appreciate both the high academic expectation communicated, and the positive learning environment facilitated by Department Heads Dr. Dyakar Penumandu and Dr. Chris Cox; and the dedication which they and many other faculty and staff maintain toward the establishment of a climate emphasis in the Environmental Engineering Department at the University of Tennessee. I also thank the department and Dr. Joshua Fu for summer support through a UT/NASA grant.

In particular, I acknowledge support from Dr. David Erickson of Oak Ridge National Laboratory (ORNL), not only in the form of assistance from an ORNL/NASA grant, and the use of the resources of the National Center for Computational Sciences at ORNL; but also in his creative scientific example, patient guidance, and steadfast confidence in my potential for the duration of this degree.

Special thanks to Dr. Lesley Ott, Dr. J. Eric Nielsen, Dr. S. Randall Kawa, and Dr. Steven Pawson of the National Aeronautics and Space Administration Goddard Space Flight Center in Greenbelt, Maryland, without whose data, communication and assistance, these projects would not have been possible.

Thanks also to Drs. Marcia Branstetter and Kate Evans of ORNL for their insight on matters scientific, diplomatic, and caffeinated.

ABSTRACT

The evolution of General Circulation Models (GCM) for climate study has led to more accurate predictions for atmospheric transport, yet precision in predictions remains in need of improvement. The National Aeronautics and Space Administration Goddard Earth Observation System model, Version 5 (GEOS-5) represents a state of the art climate model capable of simulating a wide variety of atmospheric processes informed continuously by satellite observations. This thesis examines some of the physical parameterizations employed by GEOS-5 and their effect on the transport of two greenhouse gasses: ozone and carbon dioxide.

The first is a look at the impact on ozone (O_3) distribution and transport by varying the efficiency coefficients in the background and orographic gravity wave drag parameterizations. A ten-member ensemble of simulations, each with different efficiency coefficients, is generated and compared to satellite observations and National Oceanic and Atmospheric Association NCEP reanalyses of observations. It is concluded here that the best model performance differs by season, latitude and altitude and that these considerations need to be taken into account in the code.

The second evaluates internal model variability and its contribution to differences in interhemispheric transport of carbon dioxide (CO_2). The GEOS-5 simulations incorporated CO_2 flux data from four different sources/sinks: terrestrial biosphere, ocean, biomass burning and fossil fuel emissions. CO_2 cycles at various measurement locations are compared to CarbonTracker reanalyses, and inverse flow tracing provides insight into the effects of differing initial meteorological conditions on amplitude and phasing at Southern Hemisphere sites. It is determined that for inverse modeling of arrival of species in the Southern Hemisphere, the effect of initial conditions on internal model variability is significant. Before these studies are described, however, the physics of the GEOS-5 GCM are discussed, and the relevance of each process to the studies is described.

TABLE OF CONTENTS

List of Tables

LIST OF FIGURES

CHAPTER I: INTRODUCTION

The evolution of General Circulation Models (GCM) for climate study has led to more accurate predictions for the transport of air and its constituents, yet precision in predictions remains in need of improvement. The National Aeronautics and Space Administration Goddard Earth Observation System model, Version 5 (GEOS-5) represents a state of the art climate model capable of simulating a wide variety of atmospheric processes informed continuously by satellite observations. This thesis examines some of the physical parameterizations employed by GEOS-5 and their effect on the transport of two greenhouse gasses: ozone and carbon dioxide.

The first is a look at the impact on ozone (O_3) distribution and transport by varying the efficiency coefficients in the background and orographic gravity wave drag parameterizations. A ten-member ensemble of simulations, each with different efficiency coefficients, is generated and compared to satellite observations and National Oceanic and Atmospheric Association NCEP reanalyses of observations. It is concluded here that the best model performance differs by season, latitude and altitude and that these considerations need to be taken into account in the code.

The second evaluates internal model variability and its contribution to differences in interhemispheric transport of carbon dioxide (CO_2). The GEOS-5 simulations incorporated CO_2 flux data from four different sources/sinks: terrestrial biosphere, ocean, biomass burning and fossil fuel emissions. CO_2 cycles at various measurement locations are compared to CarbonTracker reanalyses, and inverse flow tracing provides insight into the effects of differing initial meteorological conditions on amplitude and phasing at Southern Hemisphere sites. It is determined that for inverse modeling of arrival of species in the Southern Hemisphere, the effect of initial conditions on internal model variability is significant. Before these studies are described, however, the physics of the GEOS-5 GCM are discussed, and the relevance of each process to the studies is described.

CHAPTER II: BRIEF DESCRIPTION OF THE NATIONAL AERONAUTICS AND SPACE ADMINISTRATION GODDARD EARTH OBSERVATION SYSTEM MODEL, VERSION 5 (GEOS-5)

Among the more esteemed atmospheric Global Circulation Models in scientific use today is the NASA Goddard Earth Observation System model, Version 5 (GEOS-5). GEOS-5 is a weather-and-climate capable model used for atmospheric analyses, weather forecasts, uncoupled and coupled climate simulations and predictions, and for coupled chemistry-climate simulations. Two different configurations of this model were run for the two studies included in this paper, one containing stratospheric chemistry in which the effects ten different gravity wave drag treatments on ozone distribution and transport were examined, and one incorporating four different carbon dioxide flux datasets in which the influence of internal model variability on interhemispheric transport of carbon dioxide was assessed.

The Earth System Modeling Framework (ESMF)

The component-wise structure of the model is that of the Earth System Modeling Framework, ESMF (see figure reference). In this type of computational model, complicated applications are broken up into smaller pieces, or components, which are units of software composition each of which has a specific coherent function, and a standard calling interface and behavior. In this type of model, components may be assembled to create multiple applications. In addition, different implementations of a component may be available. A component is a physical domain, or a function such as a coupler or I/O system. The hierarchical tree of components can be removed at different levels accommodating experiments requiring adjustments as simple as the alteration of a single parameterization to the replacement of the entire physics package (Figure 2-1).

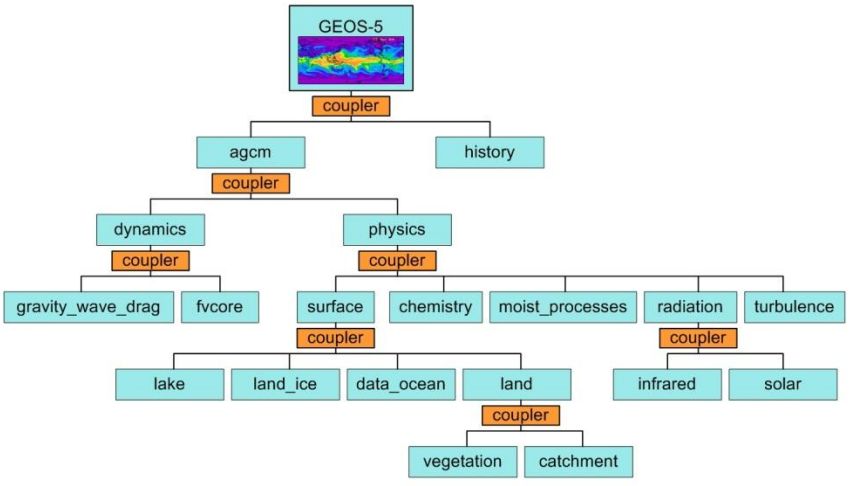

Figure 2-1. GEOS-5 ESMF Structure (http://www.earthsystemmodeling.org/about_us/)

Incremental Analysis Update

GEOS-5 is among the NASA models that synthesize diverse in-situ and satellite data streams into a single input product for model simulations. This type of forcing input is unique to the NASA models, since other agencies do not have direct access to NASA's array of real-time statellite data streams. Assimilation of this data is accomplished using "Incremental Analysis Update" (IAU) and NASA's "GSI Solver" with 3D Var (4D Var in later implementations) analysis. The IAU technique used by the GEOS-5 Data Assimilation System (DAS) was developed by Bloom et al. (1996) to minimize shocks introduced by imbalances in the mass-wind analysis component of the model. This technique helps to improve accuracy in measurement and assimilation of the processes affecting transport of ozone and other trace gases within the GEOS-5 system.

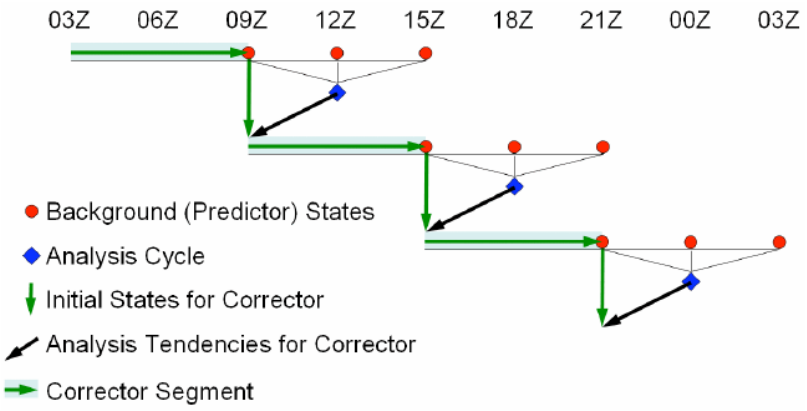

Figure 2-2. Schematic of the Incremental Analysis Update (Rieneker et al., 2008)

As shown in Figure 2-2 above, the IAU consists of four daily analysis cycles, each during which the model is run for 12 hours. The model produces both a 6-hour "corrector" segment and a 6-hour "predictor" segment which overlap during each cycle. For the "corrector" segment (green arrows), an analysis is performed every six hours using backgrounds at that time, three hours earlier, and three hours later, and observations during the six-hour period spanned by the three backgrounds. An "analysis tendency" is produced from this analysis by dividing the the results by a timescale of 6 hours. The model is then restarted from its state three hours before the analysis time, and run for six hours, adding in the time-invariant "analysis tendency" (black arrows) in addition to the model's normal physics tendencies. Following this, a "predictor" segment is produced by continuing the run without an analysis tendency for another six hours, saving the other two backgrounds (red circles) needed by the next "corrector" analysis – one at the next synoptic time and another at the end of the six hours. The entire cycle is performed four times per day. The analysis tendencies can change abruptly every six hours, but state variables are continuous (within the model's time step) solutions of the equations of motion, but contain an extra forcing term.

The GSI Solver and 3D Var Analysis

Gridpoint Statistical Interpolation (GSI) Analysis is the model that accomplishes the IAU process above for the data assimilation system. 3D Variational Analysis used in the GSI is based on the following parameterization (Kepert, 2009):

$$J(\mathbf{x}_a) = (\mathbf{x}_a - \mathbf{x}_f)^T \mathbf{B}^{-1} (\mathbf{x}_a - \mathbf{x}_f) + (H(\mathbf{x}_a) - \mathbf{y})^T \mathbf{R}^{-1} (H(\mathbf{x}_a) - \mathbf{y})$$

- $\mathbf{x}_a$ is the analysis
- $\mathbf{x}_f$ the short-term forecast
- $\mathbf{y}$ are the observations
- H produces the analysis estimate of the observed values
- $\mathbf{R}$ is the observation error covariance
- $\mathbf{B}$ is the forecast error covariance

Model Physics

The experiments undertaken in the main body chapters of this thesis dealt with variations in chemical species distribution and transport and the effect of physical and meteorological processes and their parameterizations on model representation of that transport. A brief discussion of the physical processes involved in atmospheric flow follows.

The Flux-Form Semi-Lagrangian Finite Volume Dynamical Core

The object of the flux-form Semi-Lagrangian Finite Volume Dynamical Core, central to the GEOS-5 physics structure, is to achieve consistent transport of mass, absolute vorticity, and potential vorticity; and to accomplish straightforward computation of the pressure gradient in terrain-following hybrid-sigma vertical coordinates.

The Flux Form Semi-Lagrangian Transport scheme (FFSL) developed by Lin and Rood (Lin, 2004) calculates the amount of material swept out from one time step into a given control volume (such as a horizontal grid cell), and then updates the value of a chemical constituent mixing ratio at that volume. This procedure begins by establishing a trajectory through which the particle arriving at the cell has moved during a given time step. This trajectory is found iteratively using the interpolated velocity field at the mid-point of the trajectory. From this mid-point, the departure point is calculated and the constituent mixing ratio is interpolated at the departure point using shape-preserving interpolation.

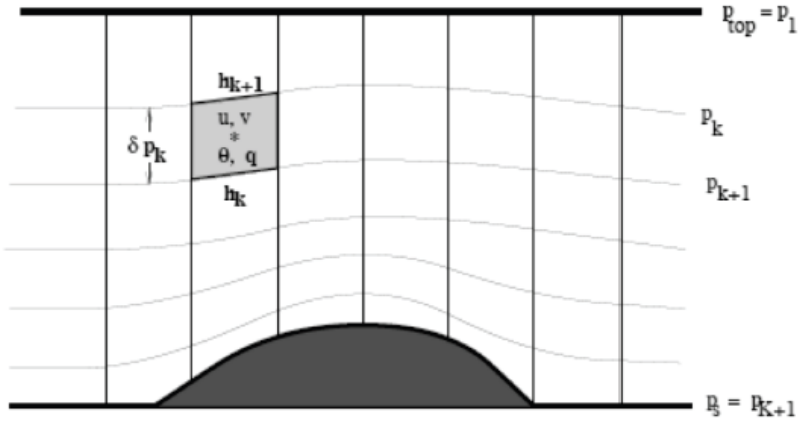

Figure 2-3. Lagrangian Control Volume (Rieneker, et al., 2008)

Thus, with the Lagrangian control-volume vertical discretization, all prognostic equations are reduced to 2D, in the sense that they are vertically decoupled. Thus, valuable computational time is saved while reasonable accuracy is maintained (Lin, 2004).

The finite-volume integration scheme used in GEOS-5 integrates around the arbitrarily shaped finite volume with each time step to determine the pressure gradient forcing and maintain the physical consistency for the finite volume under consideration. In the hybrid-sigma vertical coordinate system, the location of each finite volume top cell is allowed to fluctuate in time.

Convection

The Relaxed Arakawa-Schubert (RAS) convective parameterization estimates convective mass fluxes for a sequence of idealized convective plumes. Each plume produces mass fluxes and adjustments to the environmental profiles of zonal and meridional winds, air temperature and condensate. These are calculated sequentially by each plume (Moorthi and Suarez, 1992).

The next step, PrognoCloud**,** takes these detraining mass and condensate fluxes from RAS and adds them to the existing condensate and fraction of the anvil cloud type. Large-scale condensation is estimated using an assumed probability distribution function of the total condensate. After all sources of cloud condensate have been taken into account, four loss mechanisms are invoked: 1) evaporation of condensate and fraction, 2) autoconversion of liquid or mixed phase condensate, 3) sedimentation of frozen condensate, and 4) accretion of condensate by falling precipitation. Each of these losses is applied to both anvil and statistical cloud types. Precipitating condensates are created at the end of this step (Rieneker et al., 2008).

Clouds

GEOS-5 cloud properties and amounts are predicted at each model layer. In the radiation code, the layer clouds are grouped into three height ranges: high, middle and low, separated approximately by 400 hPa and 700 hPa pressure levels. Clouds in layers within each height group are assumed maximally overlapped, and clouds among the three height groups are assumed randomly overlapped. Different types of aerosols are allowed to co-exist in a layer. The total effective optical thickness, single-scattering albedo, and asymmetry factor of a layer are computed similarly to those of clouds (Rieneker et al., 2008).

Radiation

Atmospheric circulation arises largely from differences in heating and cooling from one horizontal or vertical region to another. These differences are caused by uneven incident solar radiation on the surface of the earth. Models of both shortwave and long wave radiation are included in GEOS-5.

Short Wave

The solar radiation model is presented in Chou and Suarez (1999). It includes the absorption due to water vapor, O_3, O_2, CO_2, clouds, and aerosols. Interactions among the absorption and scattering by clouds, aerosols, molecules (Rayleigh scattering), and the surface are fully taken into account. Fluxes are integrated over the spectrum from 0.175 μm to 10 μm.

Long Wave

Documentation of the longwave radiation model is provided in Chou et al. (2001). The parameterization includes the absorption due to major gaseous absorption (water vapor, CO_2, O_3) and most of the minor trace gases (N_2O, CH_4, CFCs), as well as clouds and aerosols with optical properties specified as input parameters.

Turbulent Mixing

Free atmospheric turbulent diffusivities are based on the gradient Richardson number. (Values in the range 10 to 0.1 are typical, with values below unity indicating significant turbulence.)

Planetary Boundary Layer

The planetary boundary layer is the lowest part of the atmosphere and its behavior is directly influenced by its contact with the planetary surface. Physical quantities such as flow velocity, temperature, and moisture display rapid fluctuations (turbulence) here, and vertical mixing is strong. Turbulent drag coefficients in the boundary layer depend on vertical stability and surface roughness (JMA, 2003).

In GEOS-5, two atmospheric boundary-layer turbulent mixing schemes are used. In Louis et al. (1982), whenever surface temperature and humidity are determined over land, the surface roughness of grassland is applied to calculations for all surface types (JMA, 2003). In GEOS-5, this scheme is used in stable situations with no clouds or with weakly-cooling planetary boundary layer (PBL) cloud. Lock et al. (2000), on the other hand, is used for unstable or cloud-topped PBLs. The Locke scheme includes a representation of non-local mixing (driven by both surface fluxes and cloud-top processes) in unstable layers, either coupled to or decoupled from the surface, and an explicit entrainment parameterization.

Gravity Wave Drag

Gravity waves, which result from the effects of the buoyancy of air in a stably stratified atmosphere, can originate from background sources (non-orographic) or from displacement of air particles due to large differences in terrain height (orographic). They propagate both vertically and horizontally and affect atmospheric flow at all latitudes and altitudes. The GEOS-5 gravity wave drag scheme is based on the National Center for Atmospheric Research (NCAR) WACCM1b parameterizations, which are in turn based on those of McFarlane (1987), Garcia and Boville (1994) and Lindzen (1981). Schemes for both orographic and non-orographic waves are employed.

The orographic gravity wave drag formulation is based on McFarlane (1987). The terrain data in GEOS-5, h(x,y), is from the GTOPO30 data with approximately 1 km resolution. The smallest scales (< 10km) are not used to force gravity waves, but enter into an orographic form drag used in the turbulence. The nominal gravity amplitude at the surface is given by MIN(h', U/N), where U is the surface wind speed and N is the low level stratification (Brunt-Vaisala) frequency (Rieneker et al., 2008).

The non-orographic waves, based on Garcia and Boville (1994), are important in the stratosphere and mesosphere, and are launched at 100 hPa. In the most current model, their amplitude is modified according to latitude and is dependent upon phase speed. It ranges from full amplitude in both polar regions (90-45 latitude bands) to 0.2 of the base amplitude in the tropics (20°S-20°N). Base amplitude is $6.4e^{-3}$ N m^{-2}. Non-orographic waves used for the simulation in the ozone study, Chapter 3 of this thesis, however, were launched instead at both 100 hPa and at 400 hPa and were modified only for latitudes 31-90N and 32-90S.

Chemical Constituents: Ozone

Rather than transporting ozone (O_3), the GEOS-5 model transports the odd-oxygen family:

$$Ox = O_3 + O(^3P) + O(^1D)$$

O*x* production rates are modified so that the ozone chemical 14 balance (Ox production rate/Ox loss frequency) agrees with ozone climatologies from the Upper Atmosphere Research Satellite data and SBUV data (Langematz, 2000). The Microwave Limb Sounder (MLS) is the instrument that measures naturally-occurring microwave thermal emission from the edge (limb) of the Earth's atmosphere and is mounted on the Upper Atmosphere Research Satellite (UARS). The instrument senses vertical profiles of atmospheric gases, temperature, pressure and cloud ice. The Solar Backscatter Ultraviolet

Radiometer (SBUV) measures the vertical distribution and total ozone in Earth's atmosphere. These instruments are flown on NOAA polar-orbiting satellites. A new Microwave Sounding Limb (MSL) is now mounted on NASA's Aura satellite which is an improved version of the UARS MLS instrument, with better spatial resolution and coverage, extended vertical range, and capability of measuring chemical constituents previously unmeasured globally from space.

Chemical Constituents: Other Constituents

The other radiatively active species include methane (CH_4), nitrous oxide (N2O), chlorofluorocarbons (CFC-11, CFC-12), hydrochlorofluorocarbon (HCFC-22), stratospheric water vapor (H2O). Additional chemistry packages can be added as needed as components of "Moist Processes" in the initial model framework.

Surface Processes

The surface processes provide surface fluxes obtained from land, ocean and sea ice models. The surface exchange of heat, moisture and momentum between the atmosphere and land, ocean or sea ice surfaces are treated with a bulk exchange formulation based on Monin-Obukhov similarity theory, which is a relationship describing the vertical behavior of non-dimensionalized mean flow and turbulence properties within the atmospheric surface layer (AMS Glossary). GEOS-5 employs specified distributions of sea surface temperatures and sea ice, either from an observed weekly/monthly mean time series or annually repeating climatological mean. The sea ice distribution is prescribed (Rieneker et al., 2008).

Studies of Physical Processes with GEOS-5

The following chapters describe two studies in which physical parameterizations in the GEOS-5 model are evaluated. The first is a direct experiment in which different combinations of efficiency coefficients are entered into the gravity wave drag parameterizations for each of ten different simulations, and the effect on ozone distribution and transport is examined. The second is more observational; that is, each of eight different simulations are run with initial meteorological conditions (prescribed by DAS) from different days in January, and differences in the CO2 cycles resulting in various regions are investigated. In each of the two studies, the other physical processes remain as they have been described here.

CHAPTER III: THE EFFECTS OF DIFFERING GRAVITY WAVE DRAG TREATMENTS ON THE SPATIAL AND TEMPORAL DISTRIBUTION OF OZONE IN GEOS-5

Melissa Allen[1], David Erickson[2], Joshua Fu[1],
Steven Pawson[3], J. Eric Nielsen[3]

[1]Department of Civil and Environmental Engineering, University of Tennessee

[2]Computational Earth Science Group, Computer Science and Mathematics Division,
Oak Ridge National Laboratory

[3]Goddard Space Flight Center National Aeronautics and Space Administration

Abstract

We analyze the effects of ten different gravity wave drag treatments on the distribution and transport of ozone by comparing 2006 GEOS-5 Global Circulation Model (GCM) output to both ground-based and satellite observation data. Global concentrations, temperatures, winds and geopotential heights in the southern hemisphere are analyzed along with vertical distributions of ozone at two (one north and one south) mid-latitude locations. We find that optimum efficiency coefficients for gravity wave drag parameterization in the GEOS-5 model depend on season, latitude and altitude. In the northern and southern mid-latitude summers of 2006, vertical profiles of both ozone and temperature are better approximated by all of the model ensemble members than they are in winter in each hemisphere, and that the treatment using the strongest southern hemisphere orographic factor best approximates the vertical temperature profile at the 42-44S, 145-147.5E (Tasmania) region. Gravity wave drag treatments with a High Latitude Background Gravity Wave Source Factor and southern orographic efficiency factor near the default values predict most closely the timing of the destruction of the Antarctic polar vortex. These findings are confirmed by the plots of strong downward ozone fluxes at 10mb and below throughout the month of December for the best-performing ensemble members. We find that measures for varying background gravity wave source, orographic factors and other tunable coefficients of gravity wave parameterization by season, latitude and altitude may produce more accurate results for the prediction of ozone distribution and transport.

This paper is under multiple-author review for submittal for publication.

3.1.0 Introduction

Atmospheric ozone distribution is neither well measured nor well enough represented in the existing climate models (Hansen, 2002). Latitudinal, seasonal and topographical differences among regions make both representation of and prediction about complex atmospheric chemistry challenging at best: relative radiation absorption and atmospheric circulation affect the flow of energy in the atmosphere, and large orographic features cause perturbations in the flow of air.

Ozone transport is accomplished by a variety of physical and dynamical processes such as atmospheric (Hadley) circulation, Brewer Dobson circulation, and planetary (Rossby) and gravity waves (Figure 3-1). Solar radiation drives the atmospheric circulation. Its energy at the equator is transported by three major northern and southern circulation cells in which the rising and falling of air results in poleward transfer and zonal winds. Most ozone production occurs in the tropical stratosphere, yet most ozone is found outside the tropics in the higher latitudes. This higher latitude ozone results from both atmospheric circulation and the slow winter stratospheric current of the Brewer Dobson circulation.

Waves in the atmosphere can be imposed on the general circulation and cause disturbances in the flow. Giant wave-like distributions of high-altitude winds called Rossby waves can arise in response to shear in atmospheric flow as air rotates with the earth. These waves are due to the variation in the Coriolis effect with latitude. Gravity waves, which result from the effects of the buoyancy of air in a stably stratified atmosphere, can originate from background sources or from displacement of air particles due to large differences in terrain height. They propagate both vertically and horizontally and affect atmospheric flow at all latitudes and altitudes. Additionally, breaking gravity waves in the "surf zone" (40-60° North and South—boundaries characterized by steep gradients in potential vorticity (PV)) in the mesosphere cause downward movement of air. Gravity waves can be caused by wind across terrestrial landforms, interaction at the velocity shear of the polar jet stream, and by radiation incident from space. Gravity waves are one of the ways in which horizontal atmospheric flow is translated to vertical flow.

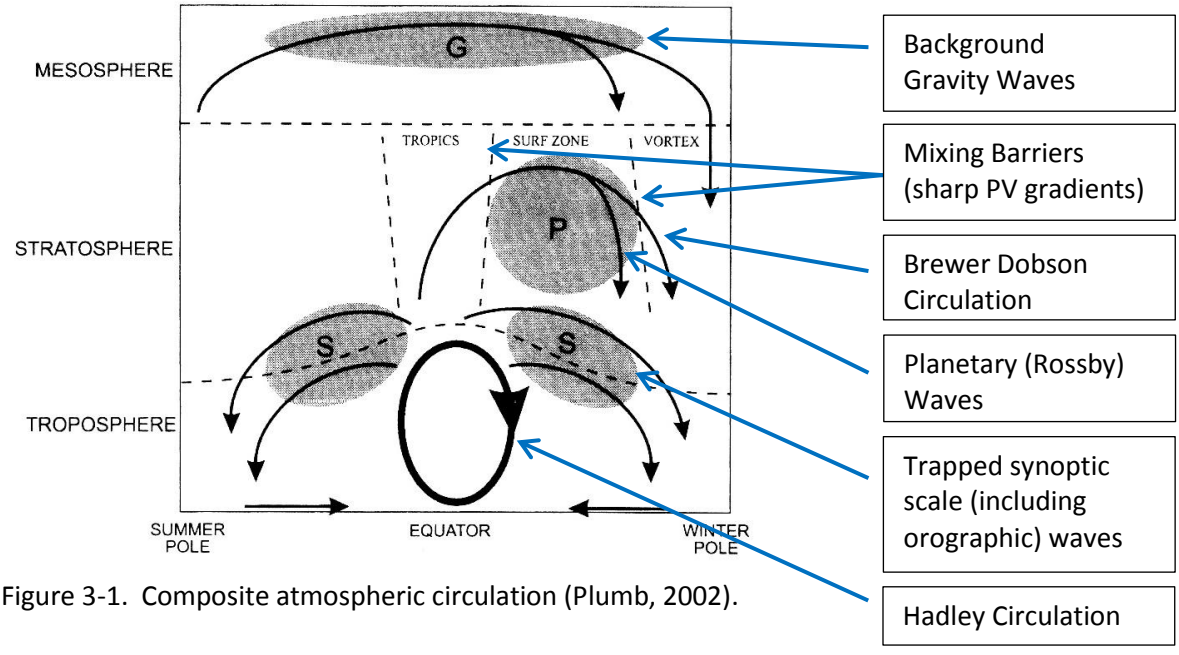

Figure 3-1. Composite atmospheric circulation (Plumb, 2002).

Gravity waves oscillate at a frequency *N* (in units of s^{-1}) described by the Brunt-Vaisala frequency:

$$\boldsymbol{N^2 = \frac{g}{\overline{\theta}} \frac{\partial \overline{\theta}}{\partial z}}$$

in which θ is the potential temperature expressed in units of Kelvin, g is the local gravitational acceleration in meters per second and z is the geometric height in meters. Under stable conditions, $N^2 > 0$, so N is real. This equation has oscillatory solutions in the form of:

$$\Delta = \Delta_1 \mathbf{cos} N\mathbf{t} + \Delta_2 \mathbf{sin} N\mathbf{t}$$

In the stable case, the restoring force associated with stratification allows the existence of waves known as internal gravity waves. Internal gravity waves are excited by horizontal winds blowing over hills and mountains and convective plumes buffeting a stable layer of air higher in the atmosphere. Internal tropospheric gravity waves of have a typical frequency of approximately 1.3E-4 s^{-2} and a period of approximately 9 minutes (Marshall and Plumb, 2008). Topographically excited gravity waves that break at the tropopause level at various latitudes are responsible for an irreversible exchange of ozone from the stratosphere to the troposphere (Lamarque et al., 1996).

Inertia-gravity waves, or background gravity waves, result from air parcel displacements resisted by both buoyancy and the rotation of the earth against inertial and gravitational stability. These gravity waves have horizontal scales greater than a few hundred kilometers and periods greater than a few hours. They are influenced by the Coriolis force, which resists horizontal parcel displacements in a rotating fluid at right angles to the horizontal parcel velocity, rather than opposite to the direction of parcel displacement, as in the buoyancy force acting in the generation of internal gravity waves. Instability in inertia-gravity waves results from an imbalance between the pressure gradient and inertial forces for a parcel displaced radially in a vortex symmetric about earth's axis (Holton, 2004).

The frequency of inertia-gravity waves satisfies the dispersion relationship:

$$\mathbf{\nu^2 = N^2 cos^2 \alpha + f^2 sin^2 \alpha}$$

with *f* = Coriolis force. In general, $N^2 > f^2$, thus inertia-gravity wave frequencies must lie in the range $f \leq |\nu| \leq N$. The frequency approaches *N* as the trajectory slope approaches the vertical, and approaches *f* as the trajectory slope approaches the horizontal. Only low frequency gravity waves, those for which the second term on the right hand side is similar in magnitude to the first term, are modified significantly by the rotation of the earth (Holton, 2004).

In the Northern Hemisphere, where *f* is positive, the flow is inertially stable provided that the absolute vorticity of the basic flow, that is, the change in momentum with respect to the change in position of the displaced air parcel, is positive. In the Southern Hemisphere, however, inertial stability requires that the absolute vorticity of the flow is negative. Generally, flow in the extratropics is inertially stable (Holton, 2004). The Antarctic polar vortex is characterized by a strong gradient in potential vorticity (the vortex edge) which is resistant to transports caused by large-scale motions, but can be influenced by transports related to smaller-scale inertia–gravity waves (Ollers et al., 2003).

We analyze the effects of ten different gravity wave drag treatments on the distribution and transport of ozone by comparing 2006 GEOS-5 Global Circulation Model (GCM) output to both ground-based and satellite observation data. The simulation comprises a control run, P2 ("Past Climate Simulation 2") and a ten-member ensemble of similar runs each with different gravity wave drag treatments based upon the parameterizations contained in the model.

Section 1 describes the model simulations and the observations to which they are compared. Section 2 outlines the methods of analysis performed, and Section 3 presents a discussion and the conclusions.

3.2.0 Model Description

3.2.1 The GEOS-5 General Circulation Model

The GEOS-5 GCM uses a flux-form semi-Lagrangian finite-volume dynamical core with floating vertical coordinate developed by Lin and Rood (Lin, 2004), which computes the dynamical tendencies of vorticity, divergence, surface pressure and a variety of selected trace constituents. The spatial resolution of the model is a 2° x 2.5° latitude/longitude grid with 72 vertical pressure levels, the top boundary at 0.01 hPa (near 80 km). At the ocean surface, temperature and sea ice distributions are specified using a global data set. Greenhouse gas and ozone depleting substance surface source gases are held constant for all of the model runs while the Hadley Center sea surface temperatures match the calendar dates of the output. The model simulations begin with the year 1949 and are run forward through the year 2010. Daily and monthly data from years 2006-2007 are selected for this study. The 50-year spin-up time provides adequate time for model meteorology to stabilize before the data are analyzed.

The GEOS-5 gravity wave drag scheme is based on the National Center for Atmospheric Research (NCAR) WACCM1b parameterizations, which are in turn based on those of McFarlane (1987), Garcia and Boville (1994) and Lindzen (1981). The orographic gravity wave drag formulation is based on McFarlane (1987). The terrain data in GEOS-5, h(x,y), is from the GTOPO30 data with approximately 1 km resolution. The non-orographic waves, based on Garcia and Boville (1994), are launched at both 100 hPa and 400 hPa for latitudes 31-90N and 32-90S. The amplitude of these waves is modified by the High Latitude Background Gravity Wave Source Factor described in section 2.0.

Ozone in the model is derived from Ox. To avoid the development of low ozone bias in the upper stratosphere, GEOS-5 Ox production rates are modified so that the ozone chemical balance agrees with the ozone climatology from the Upper Atmosphere Research Satellite (NASA) data and Solar Backscatter UltraViolet (NOAA) satellite data. The other radiatively active species include methane (CH_4), nitrous oxide (N2O), chlorofluorocarbons (CFC-11, CFC-12), hydrochlorofluorocarbon (HCFC-22), and stratospheric water vapor (H2O).

3.2.2 Observational Data

The Ozone Monitoring Instrument (OMI) total column ozone record and Microwave Limb Sounder (MLS) vertical profile data from the EOS-Aura Satellite, along with the geopotential height, zonal winds and air temperature from the National Oceanic and Atmospheric Administration (NOAA) National Centers for Environmental Predictions (NCEP) served as observational reference data sets.

3.3.0 Methods and Results

Because ozone is the major link between stratospheric chemistry and climate, its simulation is an integral metric for climate model validation. Its distribution arises from the complex interactions between transport and temperature-dependent photochemistry where the temperature depends upon

the radiative (absorption, emission and radiation scattering) effects of ozone and the transport depends upon both radiative and physical forces. Ozone concentration in the upper stratosphere is determined primarily by photochemistry, although transport due to physical processes plays an indirect role in determining concentrations because of its influence on atmospheric temperature structure. Since much less solar ultraviolet light reaches the lower stratosphere, and thus ozone lifetime at those levels is much longer, dynamical transport processes there determine the distribution more directly than chemical processes.

While the Brewer-Dobson circulation is the principal dynamical process for meridional transport of air from the tropical stratosphere to lower levels in the midlatitudes and at the poles, other physical processes, such as atmospheric waves, contribute to this transport. Among these waves are gravity waves. Gravity waves can propagate both vertically and horizontally and affect atmospheric flow at all latitudes and altitudes. We examine ten treatments (GWD10 – GWD19) of the GEOS-5 parameterizations of gravity wave drag, and the effects of these treatments on spatial ozone distribution in the stratosphere, and its total column temporal distribution in the Antarctic.

Two types of gravity wave drag are considered: background and orographic. Equations for each of these parameterizations contain tunable coefficients, three types of which are referred to as "efficiency coefficients", and another which is the square of the local Froude number. The efficiency coefficients are varied for each of the ten gravity wave drag treatments, while the square of the local Froude number (Fc^2) is kept constant at 0.5 for these simulations. Reference will be made to these coefficients throughout the paper. The orographic coefficients (ORONH and OROSH) act as constants of proportionality in determining small changes in air velocity with respect to time. These are multiplied by an established constant of 0.125 (EFFGWORO) to obtain a final efficiency factor. High Latitude Background Gravity Wave Source Factor coefficients (applied at latitudes of > 30 and < -30 with sources at both 100mb and 400mb) modify the amplitude of the background gravity waves (EFFGWBKG). Default values for the three factors are 0.6 for background, and 0.4 and 2.0 for northern and southern hemisphere orography, respectively. Table 3-1 gives the efficiency coefficient values used for each simulation along with a brief description of each.

Table 3-1. Gravity Wave Drag Coefficients

COEFFICIENT	GWD10	GWD11	GWD12	GWD13	GWD14	GWD15	GWD16	GWD17	GWD18	GWD19
EFFGWORO	0.125	0.125	0.125	0.125	0.125	0.125	0.125	0.125	0.125	0.125
EFFGWBKG	0.125	0.125	0.125	0.125	0.125	0.125	0.125	0.125	0.125	0.125
TURBPCEFFSURF	0.5	0.5	0.5	0.5	0.5	0.5	0.5	0.5	0.5	0.5
BKGGWFAC	0.600	0.600	0.600	0.600	0.600	0.400	1.000	1.000	1.000	0.600
ORONH	0.40	0.40	0.40	0.35	0.45	0.5	0.45	0.45	0.50	0.50
OROSH	2.00	2.20	1.80	2.00	2.00	2.20	1.80	1.40	1.00	2.00

EFFGWORO = Efficiency Factor Gravity Wave Orographic
This value is multiplied by ORONH or OROSH depending on the latitude to obtain the efficiency factor used for the orographic gravity wave drag.
EFFGWBKG = Efficiency Factor Gravity Wave Background
TURBPCEFFSURF = Surface Turbulence = Fc^2
BKGGWFAC = High Latitude Background Gravity Wave Source Factor
Source levels: 100mb and 400mb
Applied to latitudes >= 31 and <= -32
ORONH = Orographic Factor, Northern Hemisphere
OROSH = Orographic Factor, Southern Hemisphere

3.3.1 Vertical Distribution at Northern and Southern Wave-Breaking Latitudes

Since the midlatitudes represent the "surf zone" for non-orographic breaking gravity waves (Lamarque, et al., 2004), we begin by examining ozone and temperature profiles for locations in both northern and southern hemisphere surf zones: Erie, Pennsylvania, USA at 42-44N 80-82.5W and Tasmania at 42-44S 145-147.5E, respectively. Satellite time slice vertical profile abundances at pressure levels from 100 – 0.02 mb at the chosen locations were averaged for the months of January and July in order to examine seasonal profile differences due to temperature for each hemisphere. The values were then compared to GEOS-5 P2 (a simulation performed with GEOS-5 default settings for gravity wave drag) and GWD ensemble values for the same periods at similar pressure levels for comparison with simple linear regression.

Table 3-2. R^2 Values for MLS Vertical Ozone Distribution vs. Model Ozone Distribution, 100 – 0.02mb

R^2 Values O_3 100 – 0.02mb	P2	GWD10	GWD11	GWD12	GWD13	GWD14	GWD15	GWD16	GWD17	GWD18	GWD19
Erie January	0.355	0.427	0.450	0.408	0.509	0.512	0.459	0.567	0.537	0.485	0.474
Erie July	0.947	0.943	0.945	0.942	0.941	0.943	0.939	0.945	0.941	0.943	0.934
Tasmania January	0.930	0.913	0.913	0.914	0.909	0.914	0.911	0.922	0.921	0.927	0.915
Tasmania July	0.488	0.562	0.561	0.624	0.589	0.530	0.423	0.466	0.591	0.671	0.497

Table 3-2 shows resulting R^2 values at the 95% confidence level of comparisons of vertical ozone distribution between Microwave Limb Sounder data and the various gravity wave drag treatments of GEOS-5. The Microwave Limb Sounder (MLS) observes thermal microwave emissions from the Earth's limb at 118, 190, 240 and 640 GHz and at 2.5 THz. GEOS-5 temperature data serves as *a priori* information for the calculation of the abundances based on the radiances retrieved. According to Livesey et al. (2008), MLS ozone values at levels between 215 mb and 100 mb are calculated to a precision of ±40 ppb. At the 68 mb level, precision is ±50 ppb. According to Froidevaux et al. (2008), MLS values from 46 mb to 0.02 mb at mid to high latitudes, are within 5% difference for precision.

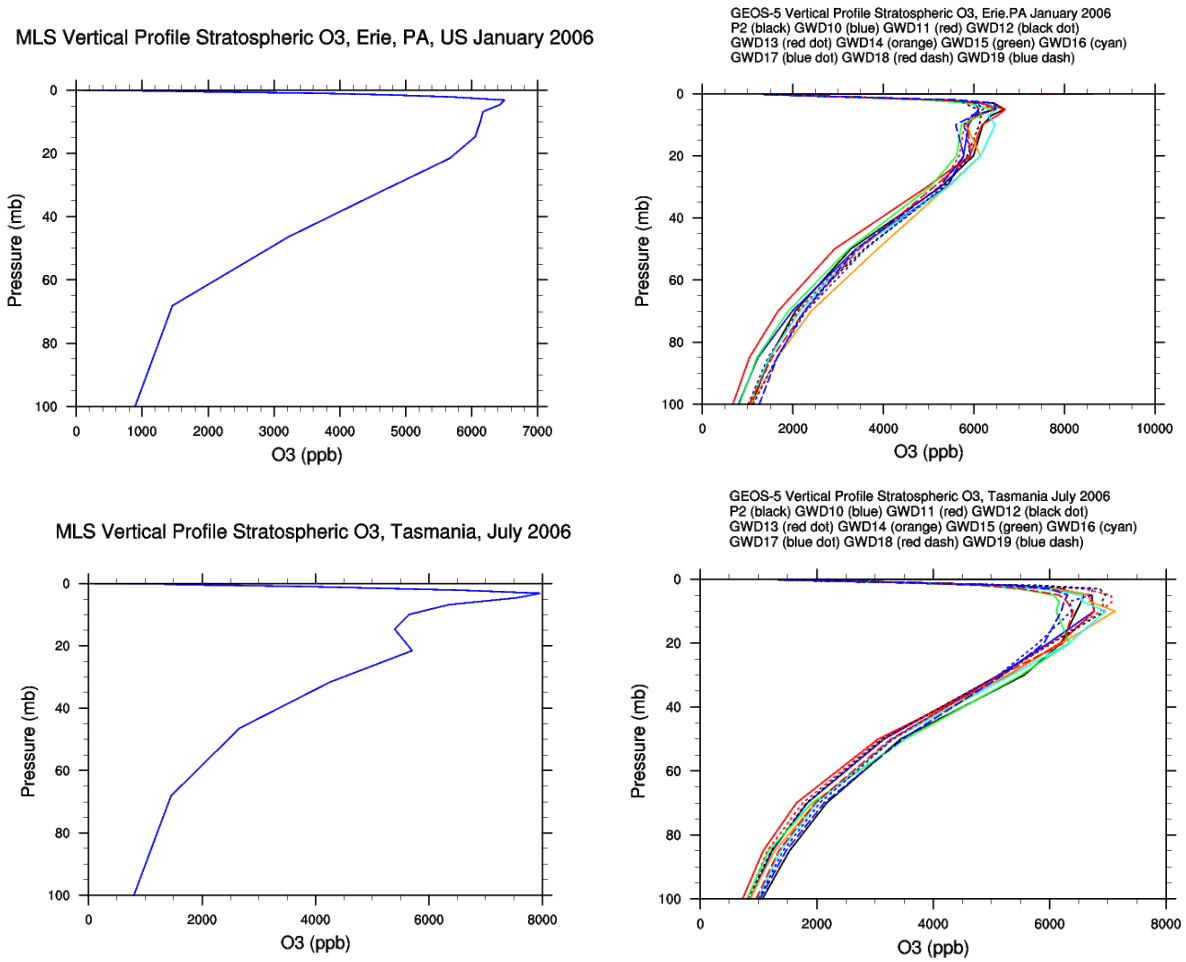

Figure 3-2. Winter 2006 Stratospheric Vertical Ozone Distribution, Erie and Tasmania

Figure 3-2 (top two panels) shows the vertical distribution of ozone for Erie, Pennsylvania for the month of January, 2006. As indicated by the R^2 value of 0.567 in Table 1, the GEOS-5 ensemble member that best predicts the vertical distribution from 100-0.02 mb is GWD16, which uses efficiency factors of 1.000 for the high latitude background gravity wave source factor and 0.45 and 1.40 for northern and southern orographic components, respectively. Maximum ozone values for the January Erie GEOS-5 ensemble reach approximately 6500 ppb at 5 mb, as does the maximum for MLS around 3 mb.

Figure 3-2 (bottom two panels) is the July 2006 vertical ozone profile for Tasmania. GWD18 performs best here with an R^2 value of 0.671. Efficiency coefficients for GWD18 are 1.0 for high latitude background gravity wave source factor, 0.5 northern hemisphere orographic factor and 1.0 southern hemisphere orographic factor.

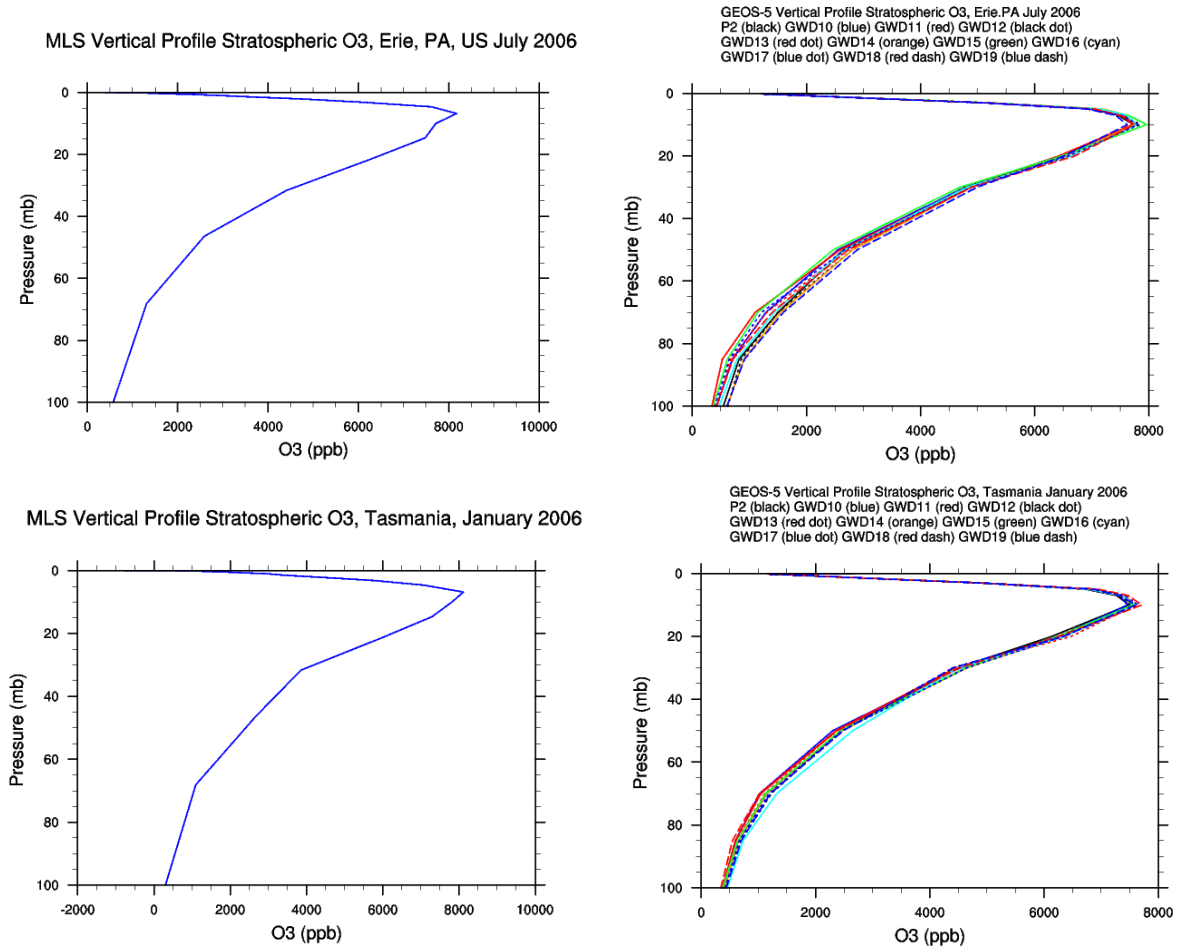

Figure 3-3. Summer 2006 Stratospheric Vertical Ozone Distribution, Erie and Tasmania

For the northern hemisphere summer location (Erie in July, 2006), Figure 3-3 (upper two panels) represents vertical ozone profiles. For the total column, the maximum value of 8200 ppb for MLS occurs around 7 mb. Maximum values between 7750 and 8000 ppb occur for the GEOS-5 ensemble at 10 mb. Although all gravity wave drag treatments show high correlation for this region and season, the overall best performing ensemble member is P2 at $R^2 = 0.947$, which uses the default gravity wave drag coefficients. Although the trends in values are similar among observational and model data, and the correlation among them is high, the individual values generated by the model underestimate those of the observations and the maxima occur at lower atmospheric levels.

The lower two panels of Figure 3-3 are vertical ozone profiles for summer (January) 2006 in Tasmania. The maximum MLS value of 8100 ppb occurs at 7 mb, whereas the maximum GEOS-5 value falls in the range of 7500 and 7750 ppb at 10 mb. Again, all gravity wave drag treatments perform well even if both the the maximum abundances and the heights at which they occur are estimated low compared to observations. P2 shows the highest correlation at $R^2 = 0.930$.

Generally, the GEOS-5 model simulations show maxima at lower abundances and at lower pressure levels than MLS does. This result could be due in part to a high bias in MLS retrieval at vertical levels 100 mb to 0.1 mb data noted by Froidevaux et al. (2008).

The simulation with no adjustment to the default gravity wave treatment performs best in the summer in both hemispheres. This may be due to a virtual absence of stratospheric waves in the geopotential field in the summer hemisphere (Cordero, et al., 2003). Wave breaking is usually most evident in winter mid-latitudes; thus, adjustment in the strength of the background gravity wave drag treatment also results in better model performance in winter at midlatitudes.

3.3.2 Temperature and Stratospheric Transport

Although photochemistry dominates ozone production in the upper stratosphere, transport in that region affects the temperature structure, which in turn has an observable effect on ozone the production (Pawson et al., 2008). In the lower stratosphere, however, where ozone lifetimes are much longer and there is far less ultravioliet light, photochemistry plays a large role only in certain geographic locations and at certain times of the year; thus, transport is the primary determinant for ozone distribution in the lower stratosphere.

The thermal structure of a Global Circulation Model (GCM) is strongly constrained by ozone (Pawson et al., 2008). Since temperatures produced by the GEOS-5 model inform the calculations of MLS ozone abundances, we evaluate the GEOS-5 GWD ensemble vertical temperature distribution performance by comparison instead with NCEP reanalysis data for the Erie, Pennsylvania and Tasmania regions. Results for comparisons of temperatures at the pressure levels considered in the vertical ozone profile, 250 – 10 mb, are shown in Figure 3-4.

NCEP temperatures in the summer hemisphere are somewhat closely approximated by all of the GEOS-5 ensemble members (Figure 3-4, right panels), whereas only a few of the members show high correlation to NCEP in the winter hemisphere (Figure 3-4, left panels). Even so, for Erie in July, lowest altitude temperatures vary by 4 degrees (228K – 232K) while highest altitude temperatures vary by 7 degrees (226K – 233K). Higher variance is seen in Tasmania in January (223K – 228k for lowest altitude and 226K -237K for highest altitude). Minimum winter temperatures at 100mb for Erie in January range from 208.5K to 213.5K and from 209K – 213.5K in Tasmania in July.

Table 3-3 gives R^2 values at the 95% confidence level for the vertical temperature profile comparisons. Of interest is the superior performance of both GWD12 (0.6 high latitude background gravity wave source factor, 0.4 northern hemisphere orographic factor and 1.8 southern hemisphere orographic factor) and GWD19 (0.6 high latitude background gravity wave source factor, 0.5 northern hemisphere orographic factor and 2.0 southern hemisphere orographic factor) for both of the summer hemispheres. Additionally, for the Tasmanian winter, only one ensemble member, GWD11 ($R^2 = 0.836$), scored an R^2 value higher than 0.5. GWD11, uses a high latitude background gravity wave source factor of 0.6, a northern hemisphere orographic factor of 0.4 and a southern hemisphere orographic factor of 2.2.

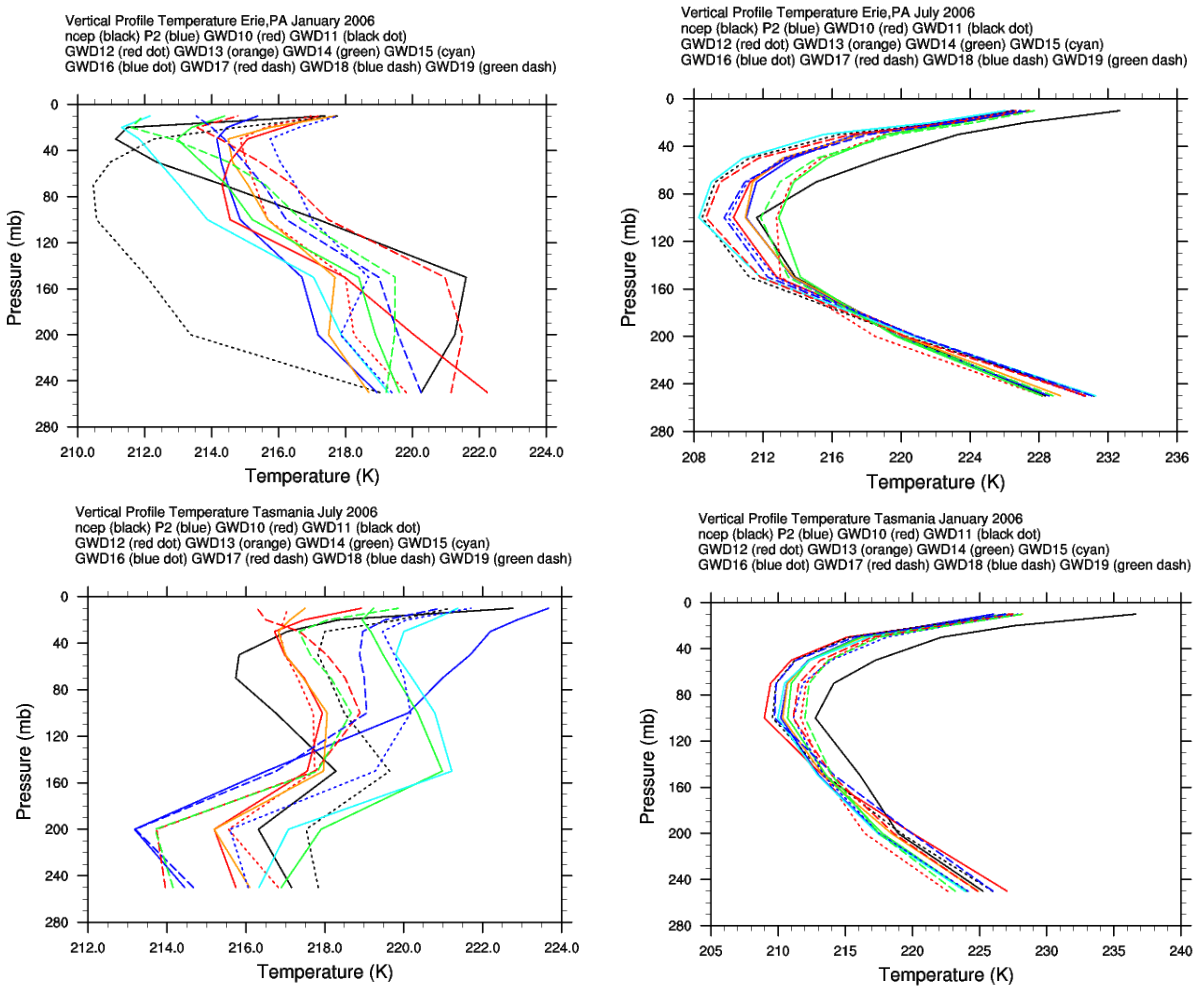

Figure 3-4. Vertical Temperature profiles, Erie and Tasmania. Summer hemisphere profiles in all of the simulations capture the trend of observations. Winter profiles vary widely among the simulations with differing gravity wave drag coefficients.

Although vertical temperature trends in the winter hemispheres are approximated only somewhat by the best performing gravity wave drag treatments, the temperature ranges of the ensemble at the lowest and highest altitudes are no wider than those of the summer hemispheres.

Table 3-3. R^2 Values for NCEP Vertical Temperature Distribution vs. Model Temperature Distribution, 100-0.02mb

R^2 Values T 215 – 0.02mb	**P2**	**GWD10**	**GWD11**	**GWD12**	**GWD13**	**GWD14**	**GWD15**	**GWD16**	**GWD17**	**GWD18**	**GWD19**
Erie January	0.703	0.542	0.094	0.754	0.745	0.849	0.762	0.794	0.823	0.684	0.689
Erie July	0.859	0.831	0.819	0.925	0.861	0.919	0.777	0.834	0.851	0.855	0.927
Tasmania January	0.874	0.767	0.797	0.965	0.889	0.892	0.918	0.940	0.887	0.785	0.957
Tasmania July	0.129	0.387	0.836	0.022	0.079	0.004	0.177	0.221	0.020	0.178	0.231

The ability of a climate model to capture temperature trends at 100 mb is important since this level is near the tropical tropopause, and it acts as the transition between chemically-controlled and dynamically-controlled distribution processes (Pawson et al., 2008). This is also the pressure level at which ozone production can be affected by surface temperature changes caused by greenhouse gases and at which it can act itself as a greenhouse gas.

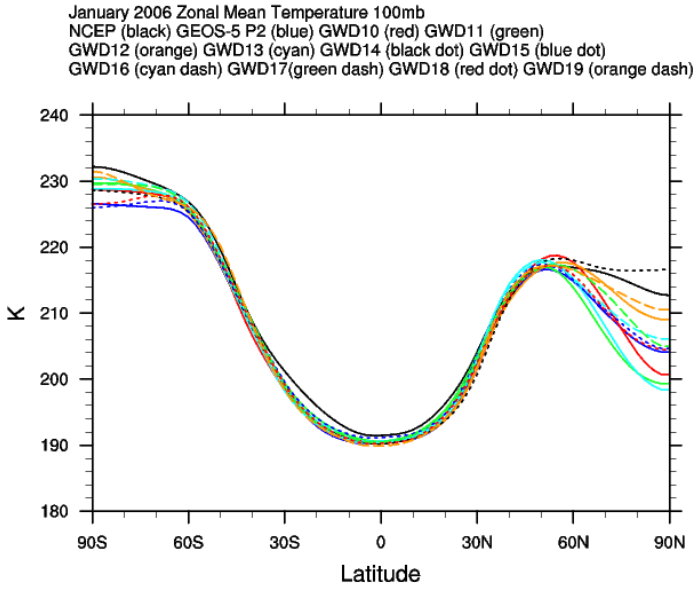

Figure 3-5. January 2006 Zonal Mean Temperature at 100mb

Figure 3-5 shows a GEOS-5 ensemble plot for January 2006 zonal mean temperature as compared to NCEP reanalyses. Although all of the GEOS-5 ensemble members show a cold bias from the South Pole to 30N, two members come closest to the NCEP data at all latitudes: GWD19 (-0.7K at the South Pole, -2.2K at the North Pole, -1.6K at the equator) and GWD12 (-1.6 at the South Pole, -3.4 at the North Pole, -1.2 at the equator). Coefficients for these treatments are GWD19: 0.6, 0.5, 2.0 for high latitude background, northern hemisphere orographic, southern hemisphere orographic and GWD12: 0.6, 0.4 and 1.8 respectively. Although P2 is among the simulations showing the largest differences in temperature from the NCEP reanalysis, it has done better at the South Pole in this simulation, but worse at the North Pole.

3.3.3 Antarctic Ozone and the Polar Vortex

Many Global Circulation Models capture the basic dynamics of the Antarctic polar vortex, yet the simulations show a late transition from winter to summer. Garcia and Boville (1994) suggest that this behavior is related to inadequate representation of gravity wave drag in the models.

Gravity waves—especially orographic waves—induce temperature oscillations which in some cases can produce temperatures low enough to generate polar stratospheric clouds, on which chemical reactions

that break down ozone must occur (Teitelbaum et al., 1994). This phenomenon also contributes significantly to mixing—the transport of air parcels by waves causes the formation of small scale vertical variations of ozone—and to the transport of chlorine and other species involved in reactions contributing to the depletion of ozone. Conditions for generation of such waves are favorable over Antarctica due to the existence of very strong winds and large orographic structures.

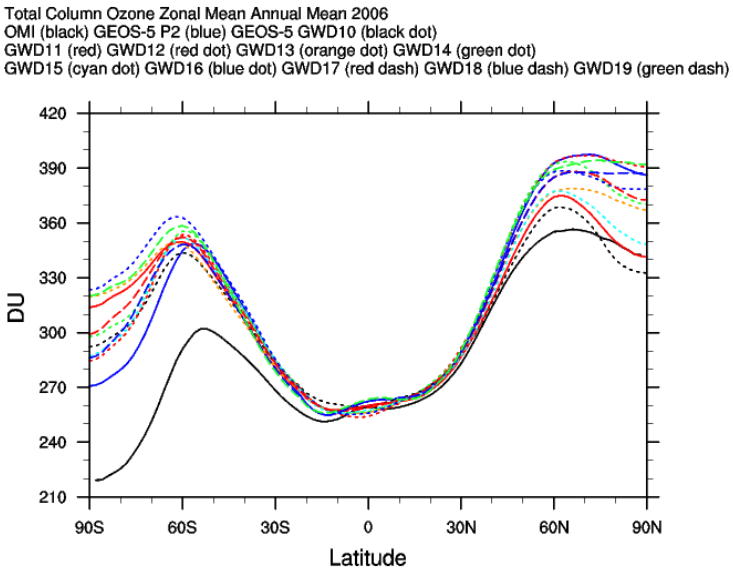

Figure 3-6. Annual Mean, Zonal Mean Total Column Ozone, 2006

Figure 3-6 depicts annual mean, zonal mean total column ozone in each of the GEOS-5 gravity wave drag simulations for the year 2006 along with satellite Ozone Monitoring Instrument (OMI) data for the same year. OMI data (solid black curve) show total column amounts of ozone reach a minimum of approximately 220 Dobson Units at the South Pole and a maximum of 350 DU at about 60N. At 55S a local maximum of 300 DU is shown dropping to a local minimum of 255 DU at 15S. Three curves in Figure 3-6 come within 10 DU of the observations at the North Pole: GWD10, GWD11, and GWD15. From about 35N to the equator, GWD10 and GWD11 follow the observations fairly closely. From 25N to the equator all GEOS-5 GCM simulations are within a few DU of the observations. All model simulations overestimate the observed values for the southern hemisphere (P2 is closest at +50DU) although all of the GEOS-5 GCM simulations follow a similar meridional trend. Northern Hemisphere efficiency factors for GWD10, GWD11, and GWD15 respectively are 0.4, 0.4 and 0.5 while southern hemisphere efficiency factors are 2.0, 2.2, and 2.2. High Latitude Background Gravity Wave Source Factors are 0.6, 0.6 and 0.4. Thus, the most successful northern hemisphere simulations use northern hemisphere orographic efficiency factors between 0.4 and 0.4 and southern hemisphere orographic efficiency factors between 2.0 and 2.2.

Southern hemisphere monthly temporal distribution of total column ozone is shown in Figure 3-7 for both observations and best-performing model simulations. OMI retrievals indicate a distinct South Pole ozone hole from September through November. The ozone hole is limited by a steep concentration

gradient, which implies that horizontal displacements due to planetary scale waves have large impacts on local measurements (Vial et al., 1995). Winds forming a polar vortex keep the ozone around the pole while ions from sea salt and anthropogenic emissions participate in ozone destruction and form the ozone hole. Reduced levels of ozone lead to a cooling at the pole, which alters the wind pattern and brings about the annihilation of the polar vortex. The beginning of this annihilation is seen in December in the OMI observations. Five GEOS-5 simulations showed similar destruction timing but with generally higher values of ozone throughout. GEOS-5 P2 shows an ozone hole in October and November. The vortex for P2 subsides in December. Although mixing ratios for all model simulations are biased high compared to OMI data, P2, along with GWD14 and GWD15 most closely resemble observations for the critical months of October, November and December. Most importantly, these simulations capture the timing of the polar vortex destruction better than the other simulations.

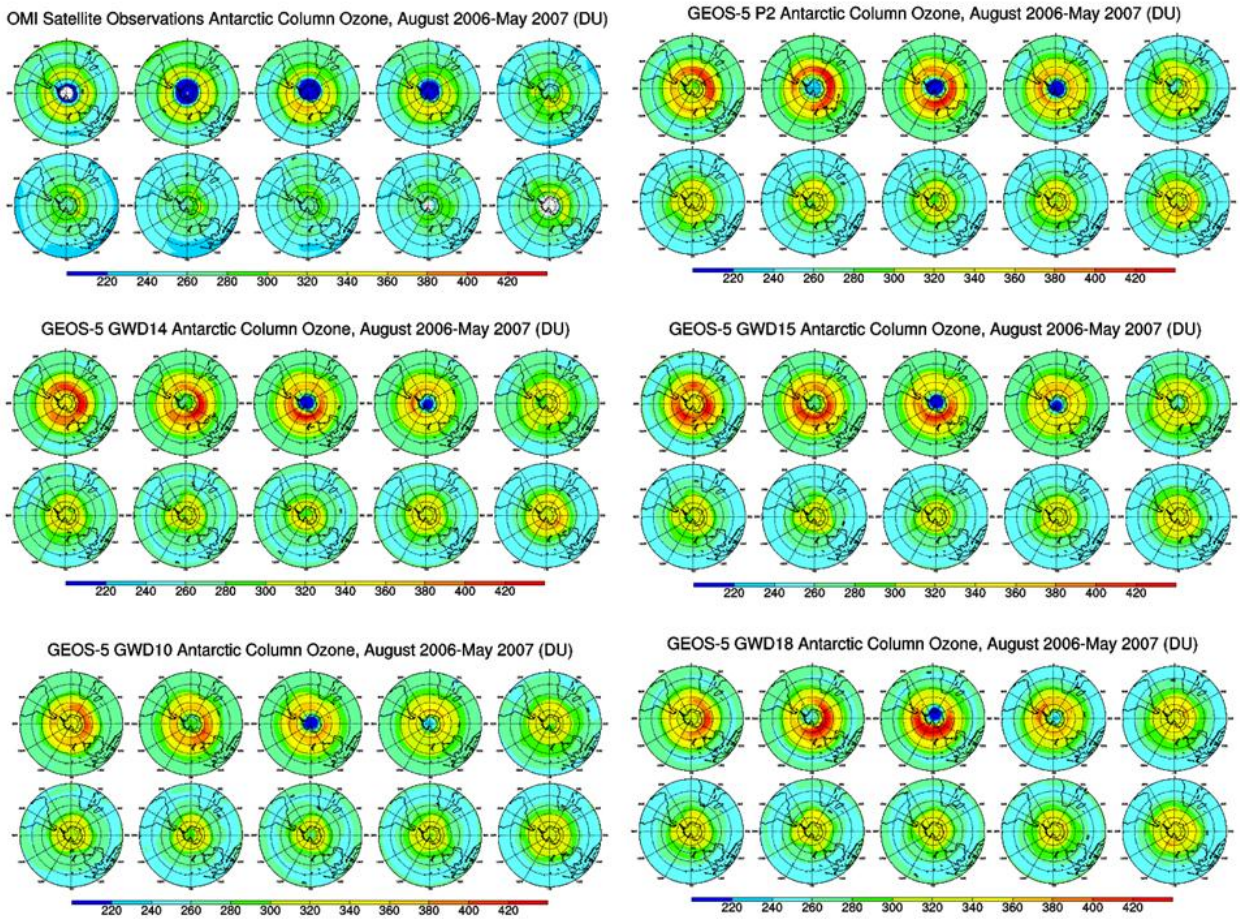

Figure 3-7. Development and Destruction of the Antarctic Ozone Hole

3.3.4 Vertical Fluxes

Stolarski et al. (2006) showed that the cause of the ozone change and the correlation between ozone increase near 20mb and the polar vortex breakdown is due to vertical fluxes over the polar cap (60-90°S). Figure 3-8 shows daily vertical fluxes for December 2006 at 60-90S for P2 and the gravity wave

drag ensemble members that best captured the timing of the polar vortex destruction for 2006-2007. Each of the five members shows negative vertical fluxes at the beginning of the month around 10mb. Between December 5th and 10th, P2 shows fluxes as great as -2 ppb m/s. GWD10 and GWD18 have flux values between -0.5 and -1 from above 10mb to below 30mb by the 10th of the month, but show only slightly negative or slightly positive fluxes after the 17th. GWD18 resumes more negative fluxes by the end of the month.

The top three panels show the results of ensemble members with negative fluxes in large vertical regions around 10mb at the beginning of the month, then still larger regions extending into the lower atmosphere as the month progresses. These three members are those which showed the best correlation to the OMI total column ozone values for August 2006 – May 2007 at 0-90S which indicated a polar vortex destruction in December of 2006. Their ozone fluxes point to increased vertical downwelling in the polar region that is associated with the polar vortex breakdown, which supports the finding of Stolarski et al. It is interesting to note the daily wave-like structure of positive and negative fluxes for GWD15.

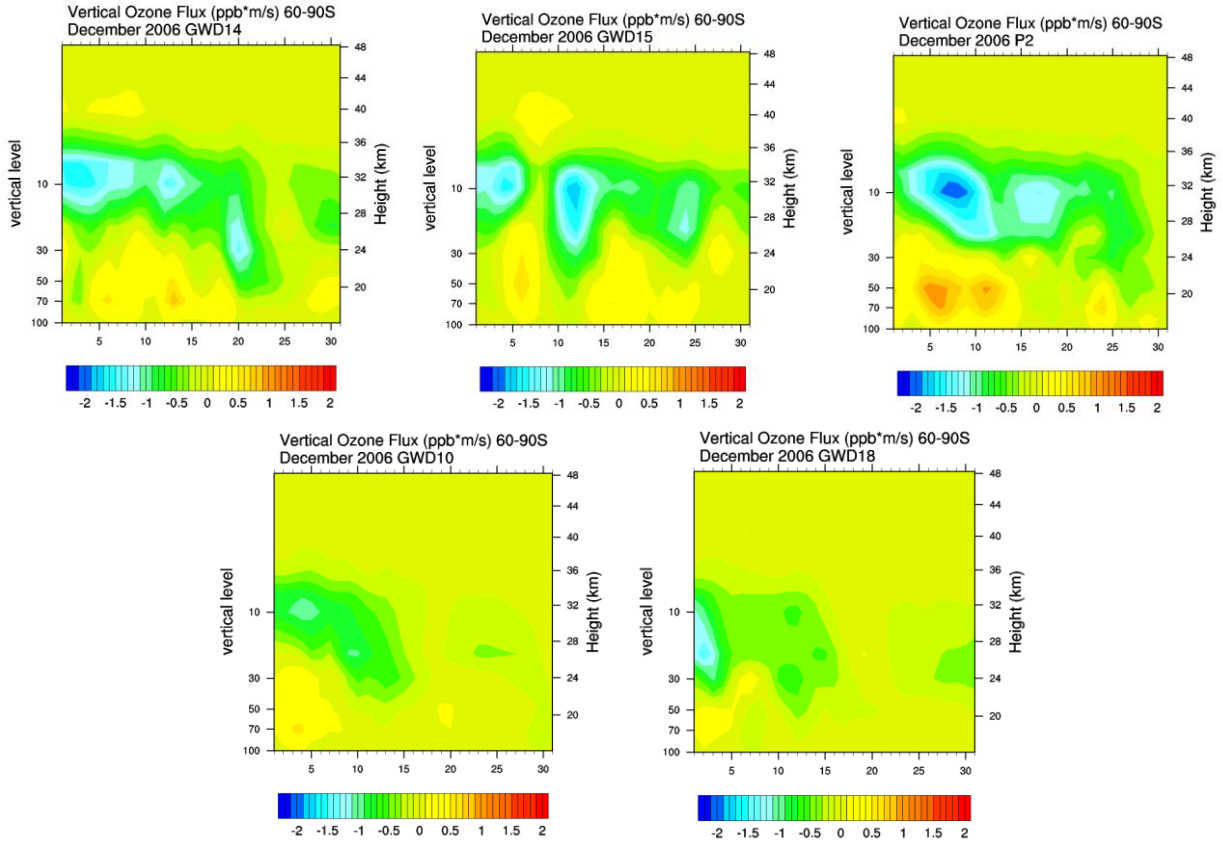

Figure 3-8. Daily Vertical Ozone Fluxes, December, 2006

3.3.5 Temperature, Zonal Wind and Geopotential Height at 500mb and 30mb Pressure Levels

Since temperature is correlated with ozone concentration, we compare temperature in the model to NCEP reanalyses at 500mb and at 30mb. Shown in the left panel of Figure 3-9 is temperature at 500mb from four of the gravity wave drag simulations with NCEP data. The trend of GWD10 most closely follows that of NCEP. Peak values occur for observations and all simulations except GWD15 in January, although simulated temperature is about 2.5K lower than the observed temperature. 2-3K differences between model simulation and observations are seen at the minima (August and May) as well. At 30mb, shown in the right panel of Figure 3-9, all four of the GEOS-5 simulations have the same values, which are slightly high compared to the NCEP data.

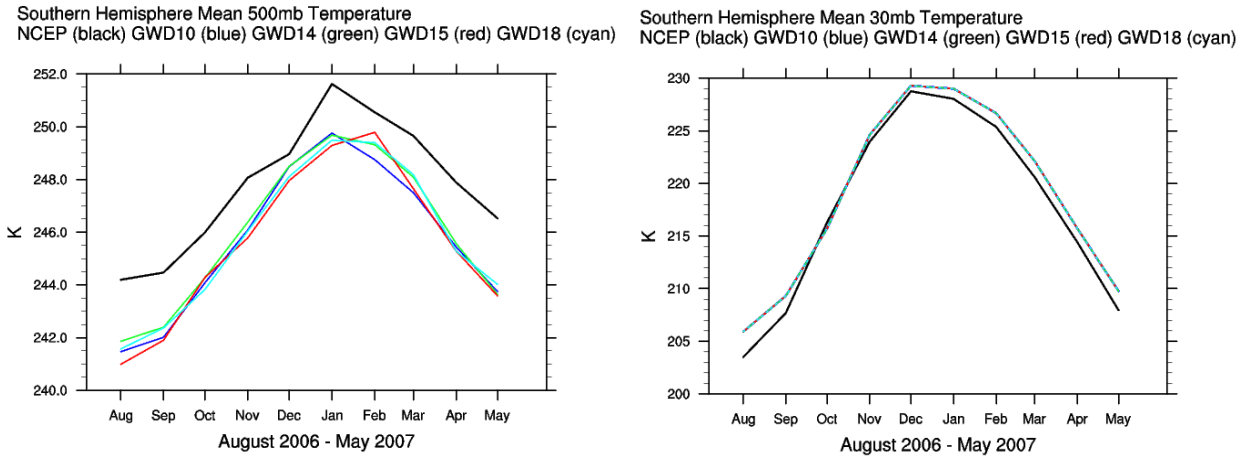

Figure 3-9. Southern Hemisphere Mean 500mb and 30mb Temperature Time Series. All of the best simulations match the NCEP data more closely at 30mb than at 500mb.

Temperature also affects geopotential height. Figure 3-10 (left) shows a comparison southern hemisphere mean 500mb geopotential height results of four simulations and the NCEP data. Two of the gravity wave drag treatments, GWD14 and GWD10 (High Latitude Background Gravity Wave Source Factors both 0.6, Southern Hemisphere Orographic Factors both 2.0, Northern hemisphere Orographic Factors 0.4 and 0.45, respectively) are within ten meters of the NCEP 500mb geopotential height for the months of December 2006 through March 2007. Figure 3-10 (right), shows that GWD18 (High Latitude Background Gravity Wave Source Factors 1.0, Southern Hemisphere Orographic Factor 1.0, Northern hemisphere Orographic Factor 0.5) makes the closest approximation to 30mb geopotential height in NCEP, although all model runs underestimate it.

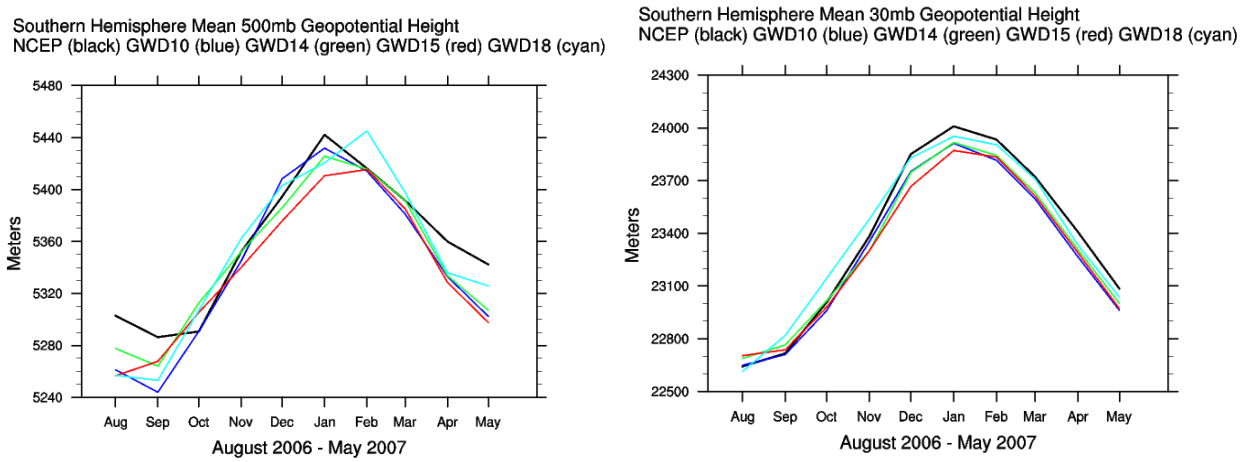

Figure 3-10. Southern Hemisphere Mean 500mb and 30mb Temperature Time Series

For the 500mb pressure level (Figure 3-11, left), NCEP data is shown in black with a minimum of 8 m/s in January and a maximum of 11.6 m/s in October. A secondary maximum of 10.4 m/s occurs in April. None of the model simulations at 500mb capture the trend of the observations, but GWD10, GWD14 and GWD15 are well within 0.1 m/s of observations at the April maximum. GWD18 shows the largest differences from the observations: 1.6 m/s in October and 1.8 m/s in February. For the 30mb pressure level (Figure 3-11, right), the GWD18 curve matches observations most closely from December into May, although speeds are slightly slower for September – November. The remaining gravity wave drag sets show higher velocities than the observations.

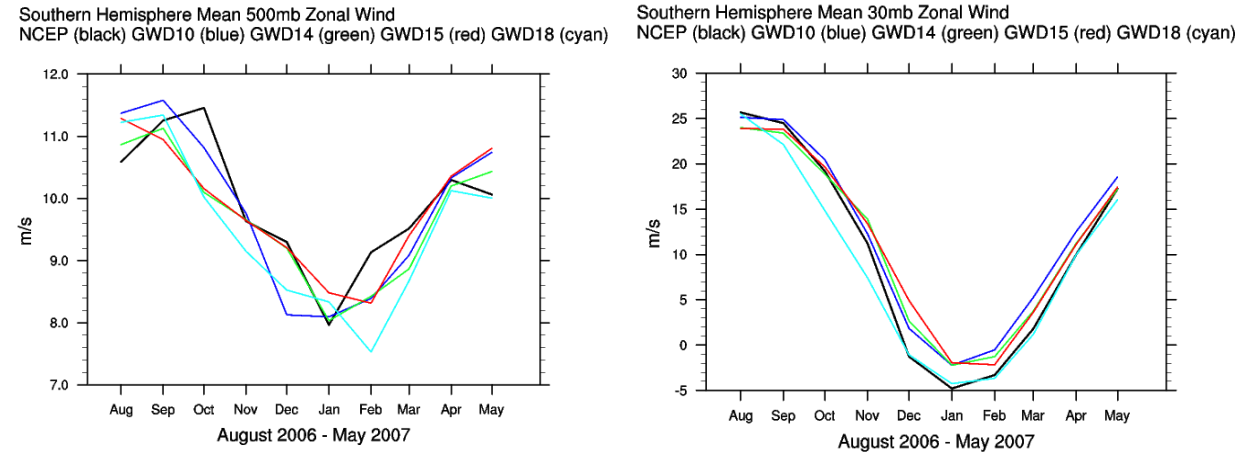

Figure 3-11. Southern Hemisphere Mean 500mb and 30mb Zonal Wind Time Series

3.3.6 Effects of Interannual Modes on Antarctic Polar Dynamics

Principal interannual fluctuations in the Antarctic polar vortex have been shown to be related to the phase changes of the Quasi Biennial Oscillation (QBO) and the Southern Annual Modes (SAM). By altering zonal winds and potential vorticity, the QBO forcing changes the refraction of planetary waves beginning in midwinter, causing the lower-stratospheric zonal average temperatures at Southern Hemisphere high latitudes to be 3–5 K warmer in the easterly phase than in the westerly during the late winter and early spring (Lait, Schoeberl, and Newman, 1989). Additionally, there is a correlation between southern hemisphere November total column ozone, and the indices associated with the principal mode of the SAM (Thompson and Solomon, 2002).

Figure 3-12 shows the relationship between the QBO and the SAM. Generally, for the years 2006-2007, both follow the same positive and negative phase trends. For the QBO, the positive phase is the easterly phase and the negative is the westerly. The QBO is essentially a 30mb tropical zonal wind anomaly index. Similarities as discussed section 3.3.5 in modeled data to observations for 30mb zonal wind may provide insight into climate effects on ozone transport from the tropics to the southern hemisphere.

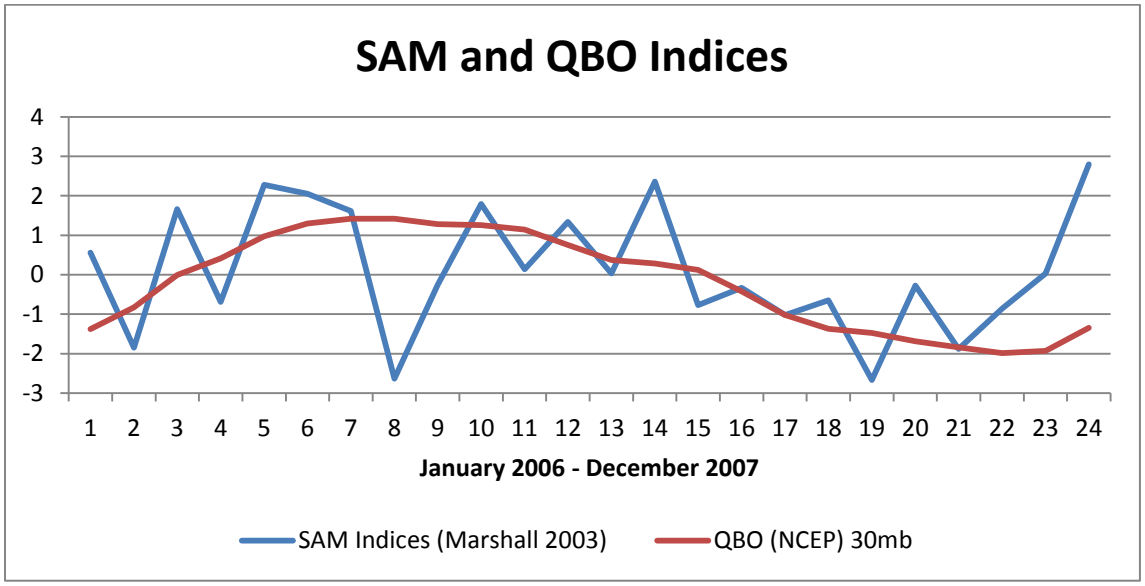

Figure 3-12. SAM and QBO indices.

Thompson and Solomon (2002) showed that the indices obtained from an empirical orthogonal function analysis for average observed 500mb geopotential height anomalies for the southern hemisphere (20-90S) for December and January serve as an inverse indices for the principal Southern Annular Mode. Likewise, seasonal anomaly values of geopotential height at the 30mb pressure level for November show a moderate correlation with December-January 500mb geopotential height anomalies and a high correlation with January-February anomalies. Further analysis of decadal time series of both 30mb zonal winds and 500mb geopotential height for the GEOS-5 data sets could show how each of the gravity wave treatments capture modal oscillations of southern hemisphere climate.

3.4.0 Conclusions and Discussion

We find that optimum efficiency coefficients for gravity wave drag parameterization in the GEOS-5 model depend on season, latitude and altitude. Likewise, for accurate long-term ozone and climate predictions, effects of interannual variation on gravity wave response may require consideration.

Seasonally, very different coefficients for gravity wave drag parameterizations proved optimum for summer and winter. In the northern and southern mid-latitude summer of 2006, the GEOS-5 P2 ensemble member, the one which uses the existing GEOS-5 gravity wave drag treatment, best approximates vertical ozone profiles. Winter ozone profiles, however, are better approximated by simulations using different sets of efficiency coefficients. For 42-44N 80-82.5W (Erie), January ozone vertical profiles are best approximated using a High Latitude Background Gravity Wave Source Factor of 1.00, a Northern Hemisphere Orographic Factor of 0.45, and a southern hemisphere orographic factor of 1.80. For Tasmania, at 42-44S 145-147.5E, a closer match in July to the MLS/Aura vertical ozone profile was achieved by using a High Latitude Background Gravity Wave Source Factor of 0.6, northern hemisphere orographic factor of 0.40 and southern hemisphere orographic factor of 1.80.

Additionally, temperature profile correlations at each mid-latitude location require different gravity wave drag efficiency coefficients. In the summer hemispheres most treatments followed the vertical temperature trend, yet those with High Latitude Background Gravity Wave Source Factor of 0.6, northern hemisphere orographic factors between 0.40 and 0.5 and southern hemisphere orographic factors between 1.80 and 2.0 performed best. Erie January best vertical temperature correlates used coefficients in the same range. For Tasmania July vertical profiles, however, only one treatment showed strong correlation: that with a southern hemisphere orographic factor of 2.2. At 100mb, the vertical level of the tropical tropopause, the treatments that performed best for vertical temperature profiles in the summer midlatitudes also approximated most closely the meridional structure of zonal mean temperature.

Varying gravity wave drag effects on ozone concentrations pertaining to the unique spatial and temporal properties of the Antarctic vortex were also analyzed. All of the model simulations overestimated the total column ozone at the Antarctic polar vortex, a result consistent with simulations performed in earlier simulations using GEOS-4. Pawson et al. (2008) found a high ozone bias at high latitudes in such a simulation, and a low bias in the upper stratosphere. In order to correct for the latter, GEOS-5 Ox production rates were modified so that the ozone chemical balance was in agreement with the ozone climatology from the Upper Atmosphere Research Satellite (NASA) data and Solar Backscatter UltraViolet (NOAA) satellite data. For best model results, an additional adjustment may need to be made to correct the high latitude total column high bias. In spite of the overestimation of Antarctic total column ozone in our simulations as well, we find that gravity wave drag treatments with a High Latitude Background Gravity Wave Source Factor of 0.60 and southern orographic efficiency factor of 2.0 predict most closely the timing of the destruction of the Antarctic polar vortex. These findings are confirmed by plots of strong downward ozone fluxes at 10mb and below during the month of December for the best-performing ensemble members.

Gravity wave drag may require different treatments for stratosphere and troposphere. 500mb NCEP values of temperature, geopotential height and zonal winds were most closely matched with treatments using a High Latitude Background Gravity Wave Source Factor of 0.6 and a southern hemisphere

orographic efficiency factor coefficient of 2.0 during the months of November, December and January. 30mb values of the same variables were better approximated with a High Latitude Background Gravity Wave Source Factor of 1.0 and Southern Hemisphere Orographic Factor of 1.0. These items noted, however, the study did not adequately evaluate variables in the troposphere because of the inadequacy of precision of the satellite data used in that vertical region. Additionally, the effects of a chemical transport component were not considered. A further comparison including these considerations would give a better understanding of the relative effects of chemistry and gravity wave dynamics on ozone distribution.

Finally, this study made use of only two years' simulations. Ten year time series and averages of various effects could give a better indication of effects that best predict long-term trends. Further analysis of decadal time series of both 30mb and 500mb geopotential height and zonal winds for the GEOS-5 data sets may show how each of the gravity wave treatments capture modal oscillations of southern hemisphere climate.

CHAPTER IV: THE INFLUENCE OF INTERNAL MODEL VARIABILITY IN GEOS-5 ON INTERHEMISPHERIC CO_2 EXCHANGE

Melissa Allen[1], David Erickson[2], Wesley Kendall[3], Joshua Fu[1],
Lesley Ott[4], Steven Pawson[4]

[1]Department of Civil and Environmental Engineering, University of Tennessee

[2]Computational Earth Science Group, Computer Science and Mathematics Division,
Oak Ridge National Laboratory

[3]Department of Computer Science, University of Tennessee

[4]Goddard Space Flight Center National Aeronautics and Space Administration

Abstract

An ensemble of eight atmospheric CO_2 simulations were completed employing the National Aeronautics and Space Administration's (NASA) Goddard Earth Observation System, Version 5 (GEOS-5) for the years 2000-2001, each with initial meteorological conditions corresponding to different days in January 2000 to examine internal model variability. Globally, the model runs show similar concentrations of CO_2 for the two years, but in regions of high CO_2 emissions due to fossil fuel emissions, large differences among the models appear. The phasing and amplitude of the CO_2 cycle at Northern Hemisphere locations in all of the ensemble members is similar to that of the CarbonTracker reanalysis. In the southern hemisphere, however, GEOS-5 model CO_2 cycles can be out of phase by as much as four months, and large variations can occur between the ensemble members. The differences vary by latitude—the most extreme differences near the tropics and the least at the South Pole. Closer examination of Cape Grim, Tasmania reveals that the CO_2 cycle for the ocean leads CarbonTracker by three months and that the amplitude of CO_2 due to biomass burning is much smaller than that of the total CO_2, thus contributing very little to the overall cycle. The most extreme differences occur among the ensemble with regard to CO_2 uptake and respiration of the terrestrial biosphere and CO2 emissions due to anthropogenic fossil fuel emissions. Integration-based flow analysis of the atmospheric circulation in the model runs shows widely varying paths of flow into the Tasmania region among the models including sources from North America, South America, South Africa, South Asia and Indonesia. For inverse modeling of CO_2 and other species in the Southern Hemisphere, the effect of initial conditions on internal model variability is significant.

This paper is under multiple-author review for submittal for publication.

4.1.0 Introduction

Internal model variability in chemical transport is important when evaluating atmospheric distributions. The chaotic nature of meteorological development, given even slight differences initial conditions, affects model representation of the CO_2 gradient and the reliability of model simulation and analysis.

Gradients in CO_2 concentration reflect sources and sinks at the surface of the earth (Heimann and Keeling 1986). Both the fossil fuel CO_2 source and natural sources and sinks of CO_2 are distributed widely over continents and oceans and they vary regularly in time and space. Historical observations made at Mauna Loa, Hawaii (Keeling et al., 1976), along with those made since at worldwide stations, indicate that patterns in atmospheric CO_2 distributions have changed non-linearly over the last 10-100 years. Erickson et al. (2008, 2011(in review)) show that these observations pose challenges for inverse studies, such as Fan, et al., (1998), and Gurney, et al. (2005), which seek those surface source/sink regions of atmospheric CO_2.

Law et al. (1996), found that the efficiency of surface interhemispheric exchange among 12 different three-dimensional atmospheric transport models showed variations in both vertical and horizontal transport, although the spatial distribution of the amplitude and the phase of seasonal cycle of surface CO_2 concentration in the Northern Hemisphere varied little between models. We examine eight different GEOS-5 model simulations of CO_2 seasonal cycles in both hemispheres given different initial meteorological conditions, and compare them with CarbonTracker reanalyses. We then assess the reasons for differences among the cycles due to regional and interhemispheric flow development.

We present first a description of the GEOS-5 model and the simulations, along with the CarbonTracker reanalysis data serving as observational data to which the model results are compared. Second, we describe the methods of analysis; and finally, we discuss results and conclusions.

4.2.0 Methods

4.2.1 GEOS-5 Model Simulations

The General Circulation Model (GCM) used to simulate variations in CO2 distribution and transport due to differences in initial meteorological conditions was that of the National Aeronautics and Space Administration's (NASA) Goddard Earth Observation System, Version 5 (GEOS-5). This model uses a flux-form semi-Lagrangian finite-volume dynamical core with floating vertical coordinate developed by Lin and Rood (Lin, 2004), which computes the dynamical tendencies of vorticity, divergence, surface pressure and a variety of selected trace constituents. Convective mass fluxes are estimates made by the Relaxed Arakawa-Schubert (RAS) convective parameterization (Moorthi and Suarez, 1992). Shortwave radiation in the model is that of Chou and Suarez (1999). Longwave radiation is documented by Chou et al. (2001). For atmospheric boundary layer turbulent mixing, two schemes are used. Louis et al. (1982) is used in stable situations with no or weakly-cooling planetary boundary layer (PBL) cloud, while Lock et al. (2000) is used for unstable or cloud-topped PBLs. Free atmospheric turbulent diffusivities are based on the gradient Richardson number.

The spatial resolution of the model is a 1° x 1.25° latitude-longitude grid with 72 vertical pressure layers that transition from terrain-following near the surface to pure pressure levels above 180 hPa. The top vertical boundary is at 0.01 hPa (near 80 km). At the ocean surface, temperature and sea ice distributions are specified using a global data set.

An eight-member ensemble of simulations using a free-running model, each initialized with meteorology from different days in January 2000 (e.g. January 1, 3, 5, 7, 9, 11, 13, 15) was performed in order to examine the effect of internal model variability on simulated trace gas distributions. The model CO2 fields were spun-up for four years prior to the beginning of the ensemble calculations. CO2 emissions are taken from the TRANSCOM Continuous experiment (Law et al., 2008). Annual CO_2 ecosystem productivity for the years 2002-2003 in this configuration is from a seasonally balanced terrestrial biosphere based on computations of net primary productivity from the Carnegie-Ames-Stanford Approach (CASA) biogeochemical model (Randerson et al., 1997). The values are distributed monthly in each of the eight model runs. Fossil fuel estimates are from the EDGAR (Olivier and Berdowski, 2001) 1990 spatial distribution scaled to 1998 country-level totals. CO_2 ocean exchange is from 1x1 monthly mean CO2 fluxes derived from sea-surface pCO2 measurements (Takahashi et al., 1999). In addition to the standard TRANSCOM protocol of fluxes, carbon emissions from biomass burning are courtesy of the Global Fire Emissions Database version 2 (GFEDv2) (Randerson, 2007; Van der Werf, 2006). Output from the model was generated daily, then daily values were averaged for each month.

4.2.2 CarbonTracker

The datasets serving as observations for model comparison are those available from CarbonTracker. Central to these reanalysis datasets are the observations of CO_2 mole fraction by the National Oceanic and Atmospheric Administration (NOAA) Earth System Research Laboratory (ESRL) and partner laboratories. Measurements of air samples for CarbonTracker are collected at surface sites in the NOAA ESRL Cooperative Global Air Sampling Network, the CSIRO Air Sampling Network and at the IPEN-CQMA sampling program where available, except those flagged for analysis or sampling problems, or those thought to be influenced by local sources. Thus, the sites for which data are available can vary each week depending on successful sampling and analysis, and each site's sampling frequency (Peters et al., 2007).

For most of the CarbonTracker quasi-continuous sampling sites, an afternoon daytime average mole fraction for each day from the time series is constructed. The atmospheric transport model in CarbonTracker does not always capture the continental nighttime stability regime; thus, its daytime well-mixed conditions better match actual values. At mountain-top sites (MLO), however, an average of nighttime hours is used since that is the most stable time period in those locations. That evaluation also avoids periods of upslope flows that contain local vegetative and/or anthropogenic influence (Peters et al., 2007). CarbonTracker samples used for this study are monthly averages of the available CarbonTracker data points for each observation location and are those that reported from 2 – 10 data points per month during the years 2000-2001 (except for Easter Island, for which February and March of 2001 consist of a single data point each).

For both the CarbonTracker reanalysis and the model runs, timeseries of average total CO_2 concentrations were generated. The annual cycle signal for these timeseries was then baseline-subtracted using a forward-differencing Fast Fourier Transform (FFT). A low-pass filter was applied to the data to remove components with a period less than 4 months. The seasonal amplitude for total atmospheric CO_2 concentrations (and for each component of that total at Cape Grim) was calculated from the difference of simulated annual maximum and minimum values of the total (or individual component) at each specified location.

4.2.3 Integration-Based Flow Analysis

The inverse analysis of flow into Cape Grim was accomplished with integration-based flow analysis techniques (Kendall et al., 2011). Integration-based flow analysis involves dropping imaginary massless particles into the flow field and then integrating the particle flow based on the velocities at each spatiotemporal point. The integration produces lines that are tangent to the flow field (i.e. field lines). Steady-state field lines are the solution to the ordinary differential equation:

$$\frac{d\boldsymbol{x}}{ds} = \boldsymbol{v}\big(\boldsymbol{x}(s)\big)\,;\ \boldsymbol{x}(0) = (x0, y0, z0) \qquad (1)$$

where **x**(s) is a 3D position in space (x, y, z) as a function of s, the parameterized distance along the streamline, and **v** is the steady-state velocity contained in the time-independent data set. Time-varying field lines utilize a 4D position in space. The equation is solved using a fourth-order Runge-Kutta integration method. While there is numerical error in the integration, fourth-order Runge-Kutta uses a

trial step at the midpoint to cancel out lower-order error terms, and it results in a practical approximation.

The GEOS-5 dataset has a time-varying hybrid-sigma pressure grid, with units in meters per second in the horizontal layers and Pascals per second in the vertical direction. Dealing with this grid in physical space involves adjusting for the curvilinear structure of the lat-lon grid and then utilizing another variable in the dataset to determine the pressure thickness at each finite volume element (voxel). A custom Runge-Kutta integration kernel was written for this purpose.

4.3.0 Results and Discussion

4.3.1 Initial Simulation Deviations

A preliminary evaluation of the eight model simulations showed first that background total CO_2 for January 2000 (Figure 4-1) in all eight simulations was between 360 and 362.5 ppm for the Southern Hemisphere and 365 and 367.5 for the Northern Hemisphere. At the equator for all models, the mixing ratio falls in between these values. The eight models also show similar regions of higher CO2 concentrations ranging from 372.5 to 400 ppm. In those regions of higher concentration, however, there are various differences in concentration values among the simulations.

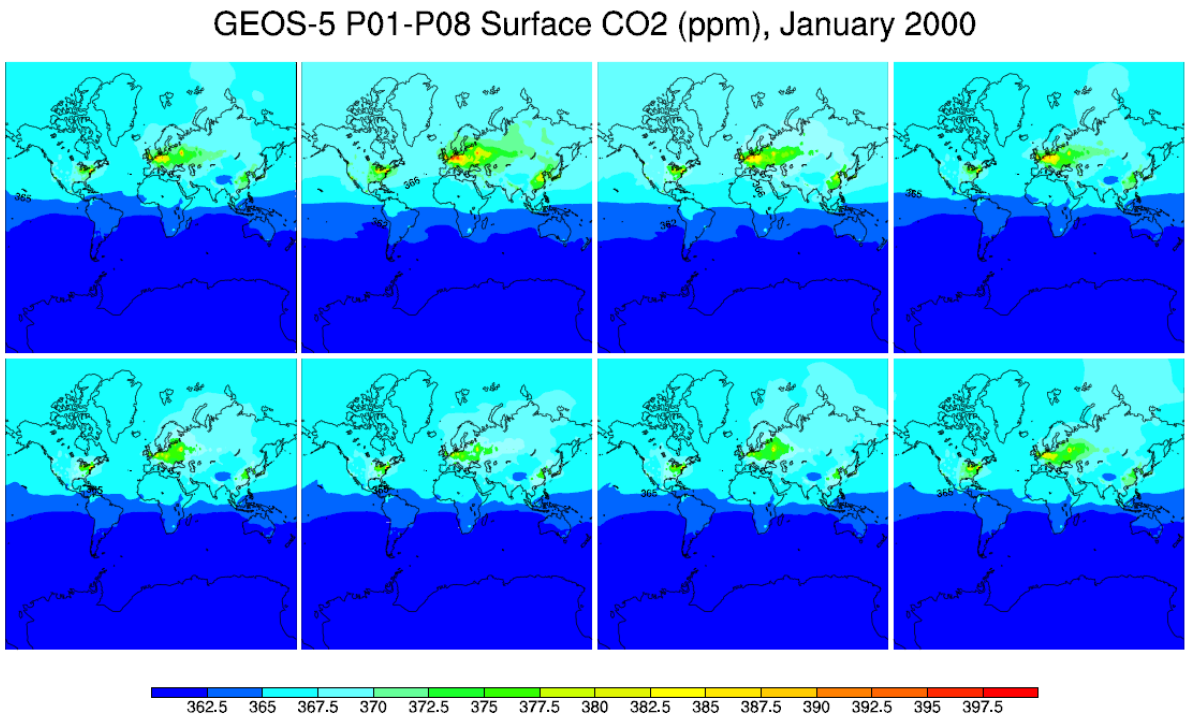

Figure 4-1. January 2000 Total CO_2 Values in Parts Per Million for Eight Model Simulations

Figures 4-2 and 4-3 depict global values for the deviations from the ensemble mean in parts-per-million for the first month of the simulation (January, 2000), and for the last month (December 2001), respectively. Maximum deviations occur at the darkly shaded locations.

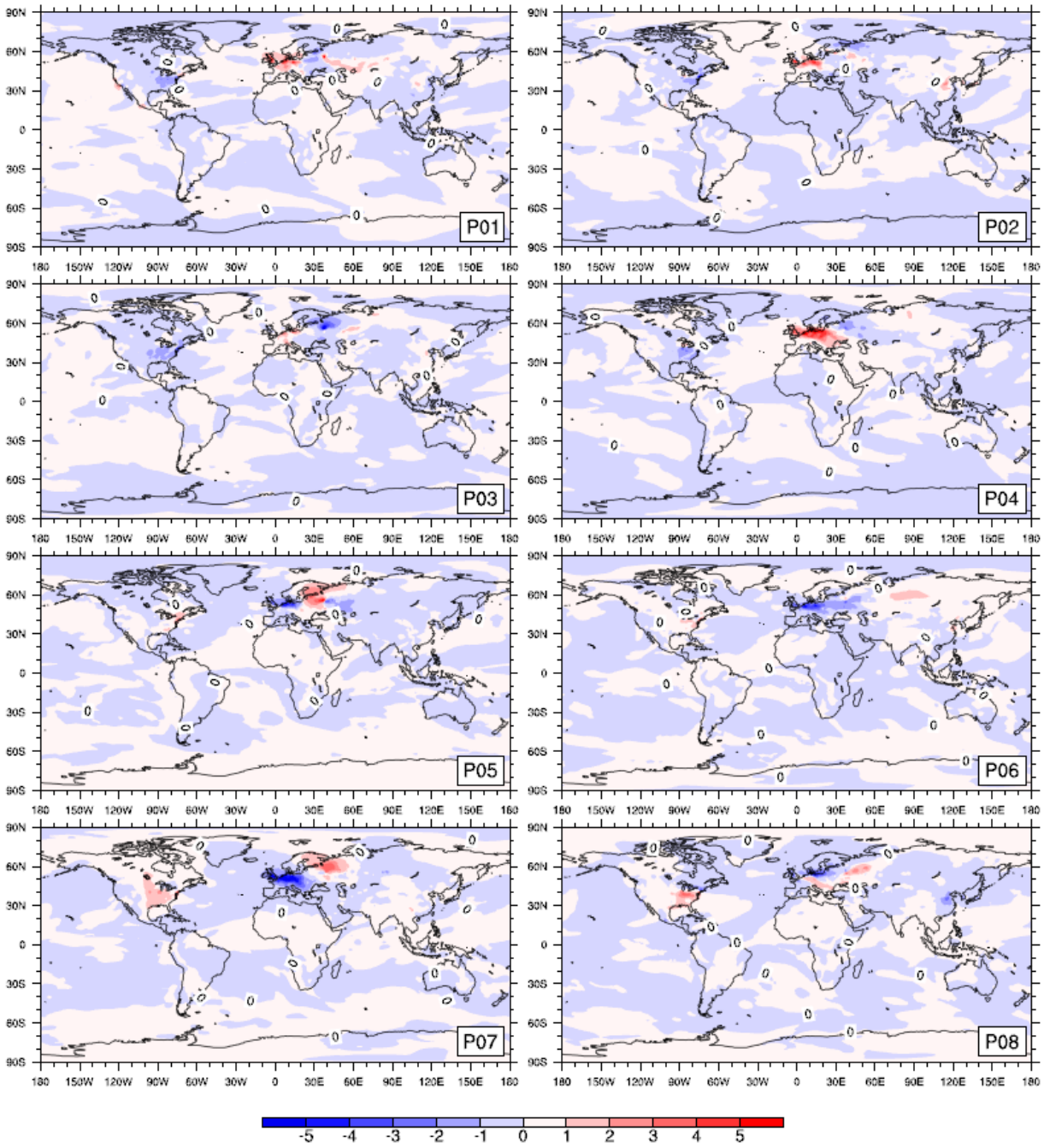

Figure 4-2. January, 2000 Values for Deviations from the Mean CO_2 from Fossil Fuel (ppm). Maximum deviations occur at the darkly shaded locations.

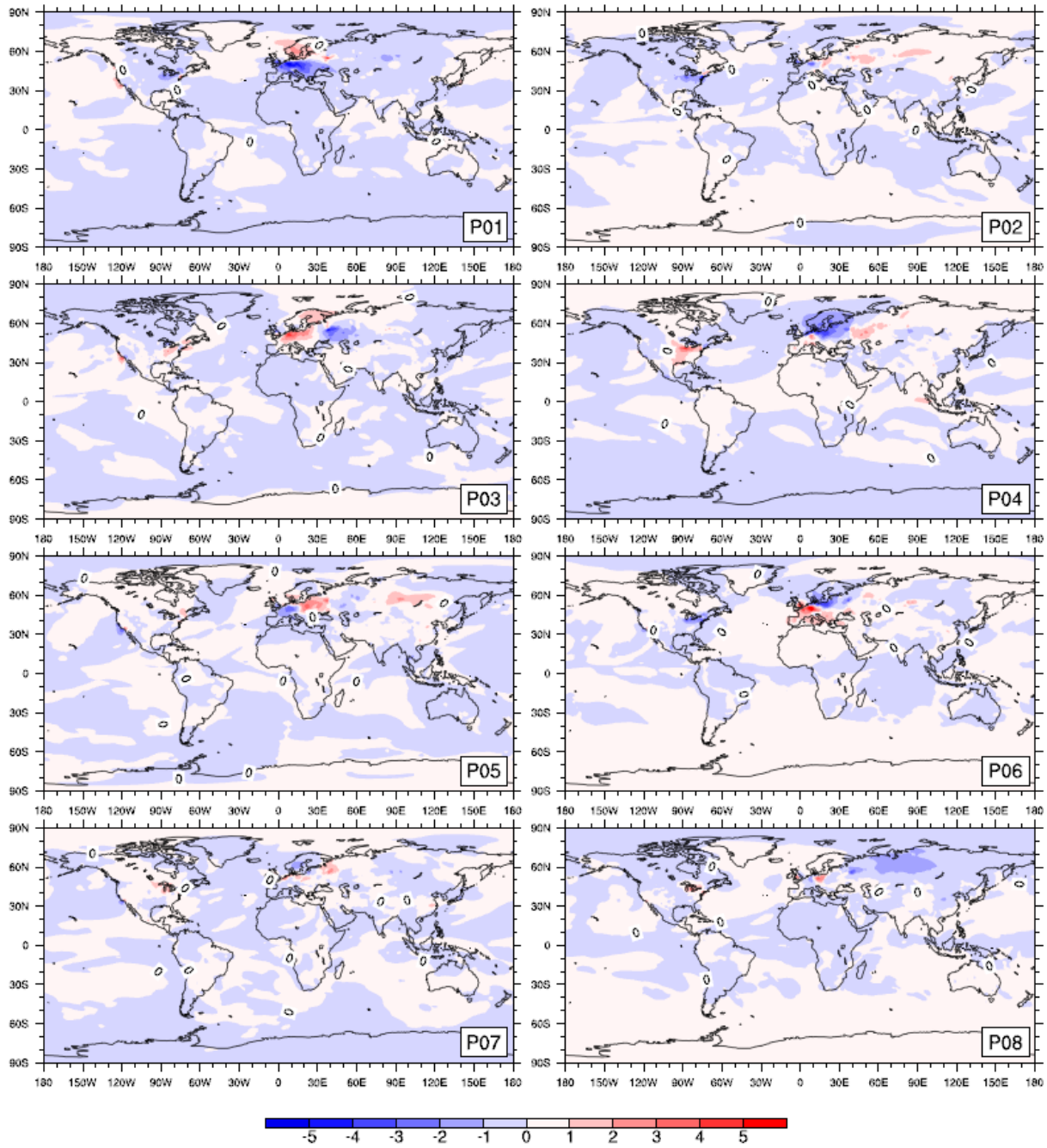

Figure 4-3. December, 2001 Values for Deviations from the Mean CO_2 from Fossil Fuel (ppm). Maximum deviations occur at the darkly shaded locations. Deviations for December 2001 are different but of the same magnitude as those of January 2000.

A quantitative description of the deviations in fractional amounts can be found in Table 4-1. The largest maximum deviation from the mean for January, 2000 (+21%) occurs in simulation P04 in the region of Germany/Poland, and the smallest (7%) in P06—a discrepancy of a factor of 3. In December 2001, the

maximum deviation (+22.5%) occurs at the same location in simulation P06, in which the region showed a negative deviation in January 2000. The smallest maximum deviation for this month (7%) is also ~1/3 of the largest. Mean deviation from the mean for all simulations, while low (0.005% to 0.26%), and somewhat variable (least and greatest differ by two orders of magnitude in January 2000 and one order of magnitude in December 2001), nevertheless persists from the first month of the run until the last, suggesting that the simulations tend not to further stabilize in two years' time.

Table 4-1. CO_2 Fossil Fuel Emissions, Mean and Maximum Deviations from Ensemble Mean Values

Ensemble Member	Mean Deviation Jan 2000	Max Deviation Jan 2000	Mean Deviation Dec 2001	Max Deviation Dec 2001
P01	0.0010447779	0.1987460532	-0.0024473974	0.1390163346
P02	-0.0007079733	0.1594262739	0.0010350785	0.0701868561
P03	-0.0001030051	0.1015154389	-0.0005215160	0.1248158015
P04	9.8400155e-05	0.2117673279	0.0004498687	0.1444526864
P05	-0.0003401078	0.2023678019	0.0003891951	0.1083048087
P06	-0.0011610277	0.0788179804	0.0026228091	0.2250762132
P07	0.0011200552	0.1791553609	0.0001354068	0.1088921124
P08	4.8880779e-05	0.1472506528	-0.0016634449	0.1099138499

4.3.2 CO_2 Cycle Phase and Amplitude

The uptake and release of atmospheric CO_2 with various surface carbon reservoirs imparts a strong signal on observed atmospheric CO_2 concentrations on time scales ranging from days to years (Erickson et al., 1996). To simulate these exchanges with the model, the CO_2 configuration for GEOS-5 provides input for the most important flux conditions: terrestrial biosphere, ocean, fossil fuel combustion and biomass burning. It is known that the overall seasonal cycle of all sources and sinks is dominated by variation in atmosphere-terrestrial biosphere CO_2 exchange (Heiman, Keeling 1996, Erickson et al., 1996), but recent studies evidence the continually emerging fingerprint of fossil fuel emissions on both global and regional cycles (Erickson et al., 2011).

In Figure 4-4, Northern Hemisphere CO_2 cycles simulated by the model are generally in phase with the CarbonTracker data although the amplitudes are underestimated by the model at both Romania and Kazakhstan, and the June 2000 minimum for the CarbonTracker data in Romania leads the models by one month. Model amplitudes at Park Falls, Wisconsin overestimate CarbonTracker especially during the latter half of 2000 and at the July-August minimum in 2001. At Mauna Loa, the models show slightly larger amplitudes but very similar phasing for 2000, and very near matches for amplitude and phase in 2001. These similarities among model runs and observations suggest that both physical parameterizations and CO2 flux sources are administered reasonably for the Northern Hemisphere and that the differing initial conditions in meteorology in the eight ensemble runs have little effect on the realization of the CO_2 cycle in these latitudes.

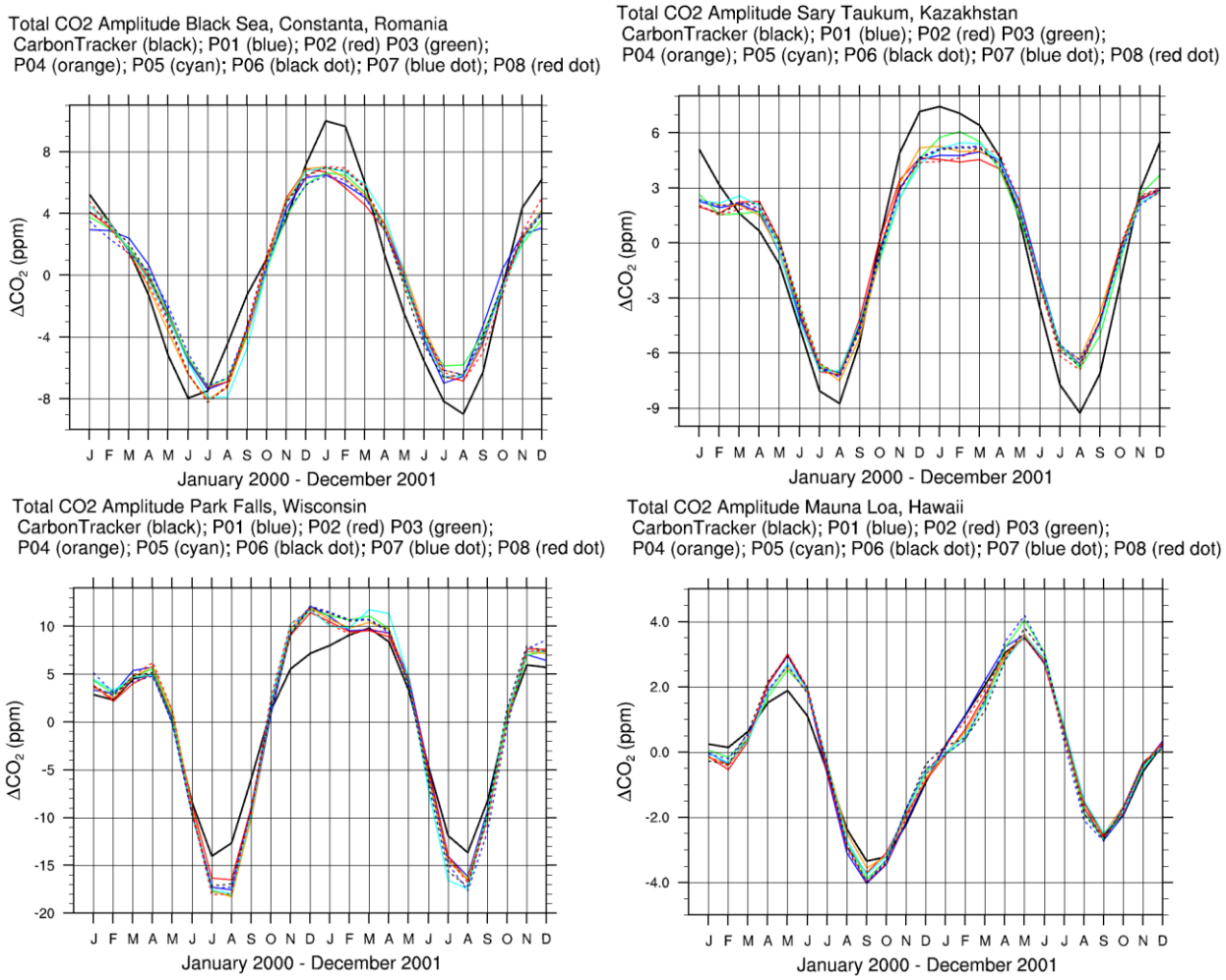

Figure 4-4. Northern Hemisphere CO_2 Cycles, CarbonTracker vs. Model Ensemble

Results for the Southern Hemisphere in Figure 4-5 show marked differences in both amplitude and phasing among the models and with regard to the CarbonTracker reanalysis data set. In fact, the number of months difference in phase for models compared to reanalysis differs according to latitude—the farther north in the southern hemisphere, the farther out of phase. For example, at Easter Island (coordinates: 27.15S, 109.45W), the models lead the observations by four months; at Cape Grim, Tasmania (40.68S, 143.68E), by three months; at Maquarie Island (54.48S, 158.97E), by one month; and at the South Pole by less than a month.

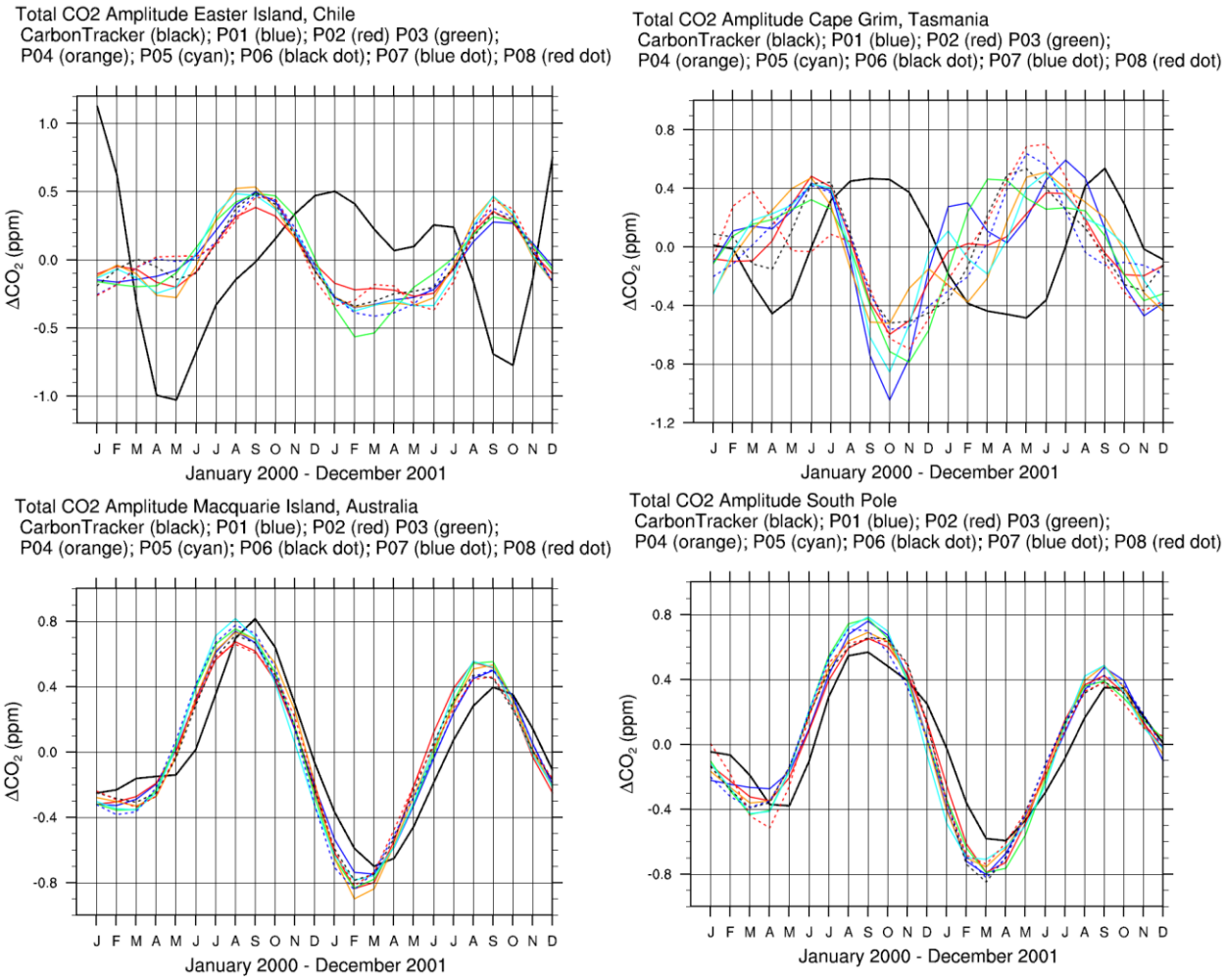

Figure 4-5. Southern Hemisphere CO_2 Cycles, CarbonTracker vs. Model Ensemble. Upper: Easter Island and Cape Grim, Tasmania show model phase and amplitude differences. Lower: Macquarie Island and the South Pole show better model agreement with CarbonTracker.

To better understand the cause of the widely differing model simulations for Cape Grim, the FFT procedure performed on the total CO_2 cycle for all of the locations in the study was employed for each component of the total CO_2 concentration at Cape Grim and compared to the CarbonTracker data for the region. Figure 4-6 shows that biomass burning has little effect on the cycle, that the ocean cycle leads the observations by three months (as in Kawa et al., 2004), and that both the terrestrial biosphere (CASAM) and the fossil fuel cycles are affected quite differently by the propagation of the differing initial meteorological conditions applied to each model ensemble member.

The fossil fuel component of the CO_2 cycle here is the only component that is more or less in phase with the observations (especially for ensemble members P01 and P02, identical for this component and represented by the red curve), which is consistent with Kawa et al.(2004). The amplitude of this signal is approximately 30% of the total CO_2 signal in the observations, consistent with Erickson et al. (2011) in which the National Center for Atmospheric Research (NCAR) Community Atmosphere Model, Version

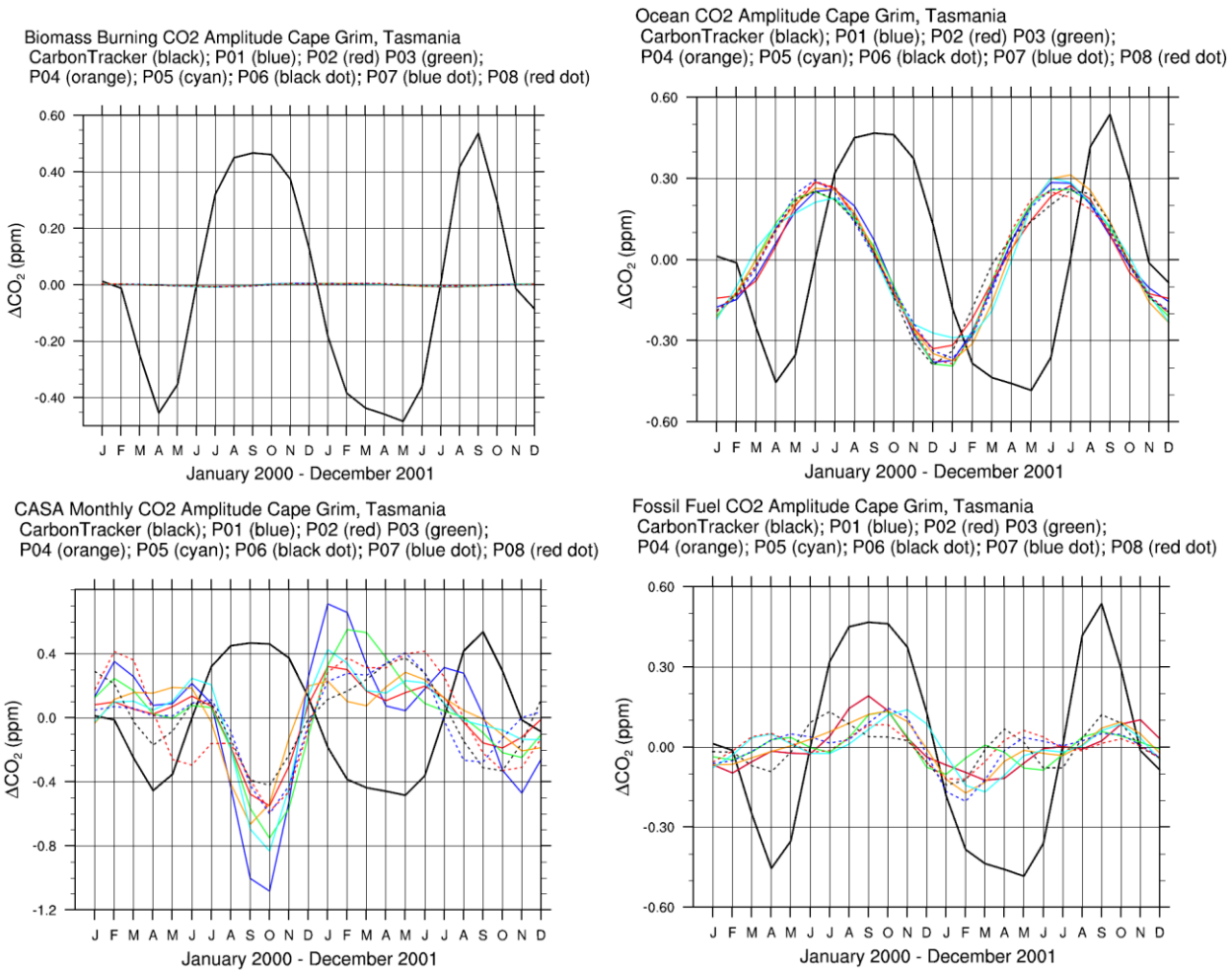

Figure 4-6. Cape Grim Components of the CO_2 cycle

4.0, was run with a monthly fossil fuel flux data set updated in 2011 from Andres, 1996. These findings suggest that although interhemispheric transport of CO_2 from fossil fuel from the Northern Hemisphere to the Southern Hemisphere may affect the phase of the CO_2 cycle in the Southern Hemisphere; internal model variability still obstructs the true fossil fuel CO_2 signal at specific sites in the Southern Hemisphere.

Observations of long-lived tracers indicate that the time required for mixing tropospheric air between the Northern and Southern Hemisphere extratropics is on the order of 0.61 – 1.4 year (Kawa et al., 2004, Denning et al., 1999, Bowman and Cohen, 1997, Heimann and Keeling, 1986). Denning et al. (1998), found that differences in vertical structure among general circulation models dominate the differences in true interhemispheric exchange. We investigate differences in both vertical and horizontal structures developed from differing initial conditions that may be responsible for similar transport discrepancies.

To gain insight into the effect of these meteorological systems on atmospheric flow (and resultant species transport) from the Northern Hemisphere to the Southern Hemisphere and ultimately into Cape Grim, a 3D time-varying flow analysis was performed using a method of integration-based flow analysis.

4.3.3 Flow into Cape Grim

To determine the historical path of a given particle arriving at Cape Grim, equation (1) in section 2.3 is solved using a negative time step (= 14,400 seconds or 4 days), and the integration progresses backward through space and time. In these analyses the lower 13 pressure layers (approximately 1013 hPa to 820 hPa if the lowest layer is at sea level) were queried for, and particle tracers initialized from each of those queried points. The destination location was set to the lower 13 pressure layers of the Cape Grim.

Figures 4-7 through 4-9 show arrivals of air into Cape Grim after 1 month travel time for the months of January, May and July, 2001, respectively. Each color represents the trajectory computed by each model simulation. Opacity corresponds to time elapsed—the more transparent, the longer temporal displacement.

January 2001 is depicted in Figure 4-7 (left). Brown (P07) and black (P08) trajectories are not seen in the South Pacific vortex (circled). This indicates that in these simulations parcel arrivals are from locations (primarily Australia) closer to the destination. The panel on the right is a close-up of the arrivals of air for each model at Tasmania in January 2001. Each ensemble member shows an approach from a different direction. Opacity corresponds to time elapsed—the more transparent, the longer temporal displacement.

May 2001 arrivals with one-month lead time are portrayed in Figure 4-8. Streams from blue (P03), purple (P02), red (P01) and cyan (P04) arrive latest at Cape Grim, since these come from the farthest away. Black (P08) spins in a tight vortex around Tasmania while the other simulations rotate nearer the southern Australian coast. One month pathways to arrival at Cape Grim in July are illustrated in Figure 4-9. Purple (P02), yellow (P07), green (P05) and blue (P03) paths show tendrils reaching back to Brazil, South Africa and Indonesia, respectively.

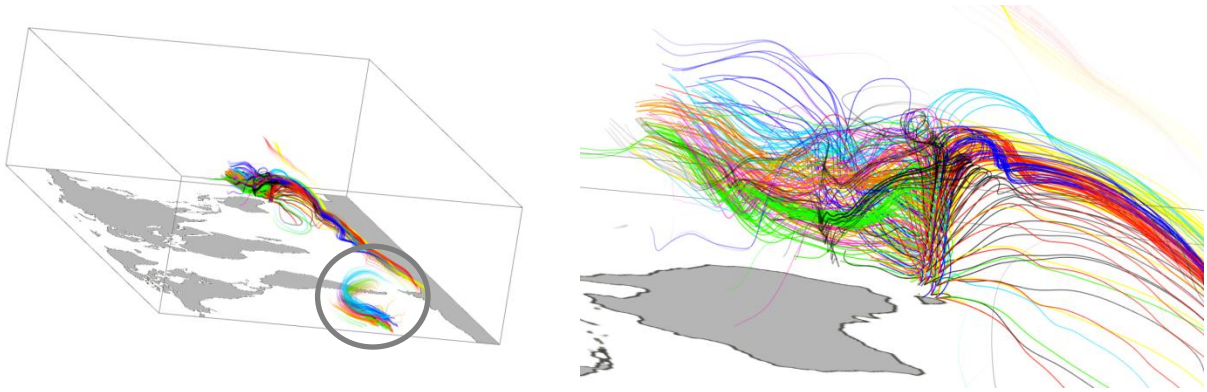

Figure 4-7. January 2001 Arrivals into Cape Grim with One Month Lead Time, Global and Arrival Point

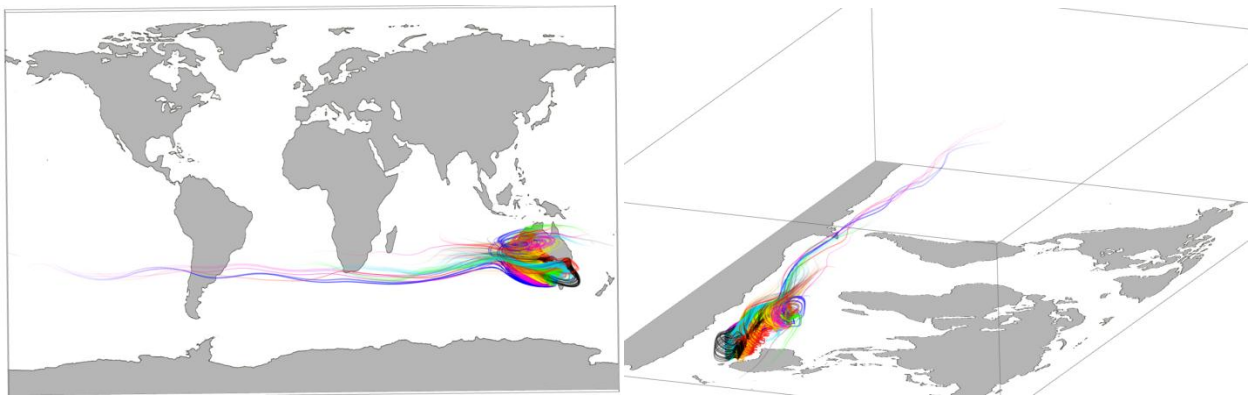

Figure 4-8. Two Views of May 2001 Arrivals into Cape Grim with One Month Lead Time

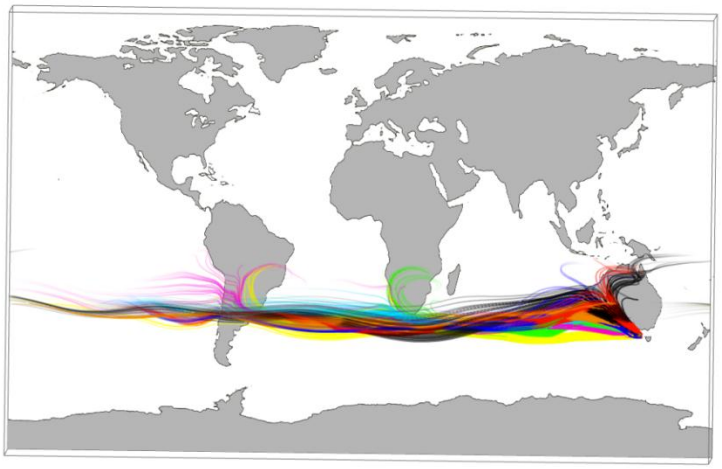

Figure 4-9. July 2001 Arrivals into Cape Grim with One Month Lead Time

For the examination of potential paths from the Northern Hemisphere to Cape Grim, a similar procedure was used to compute particle paths with three month lead time. For January 2001, shown in Figure 4-10, all models indicate air parcels entering Cape Grim from the vortex in the South Pacific, but P02, P03, P05 and P07 show larger amounts of air entering from this source. P01, P06 and P08 display airstreams primarily influenced by the Southern Ocean "winds of infinite fetch".

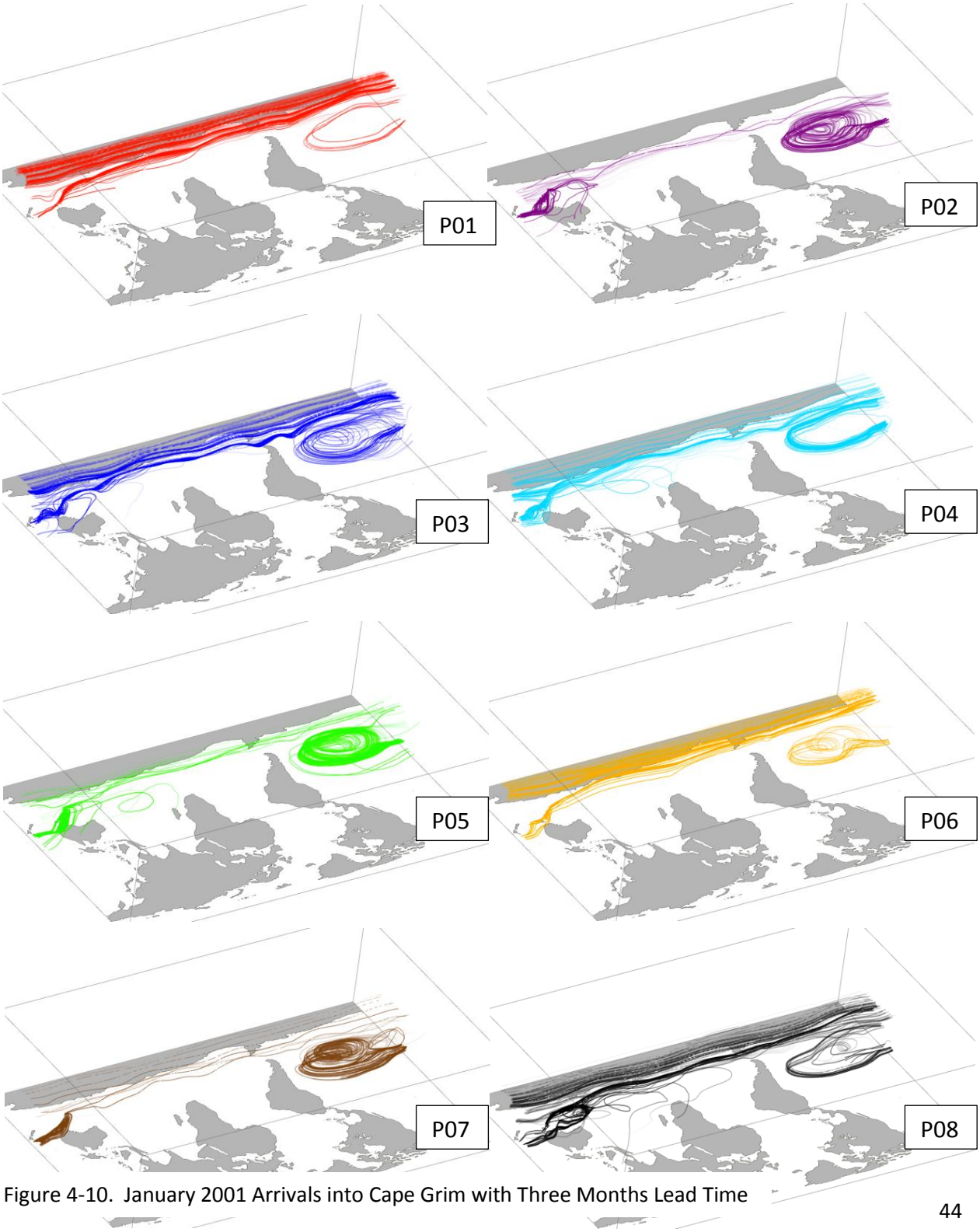

Figure 4-10. January 2001 Arrivals into Cape Grim with Three Months Lead Time

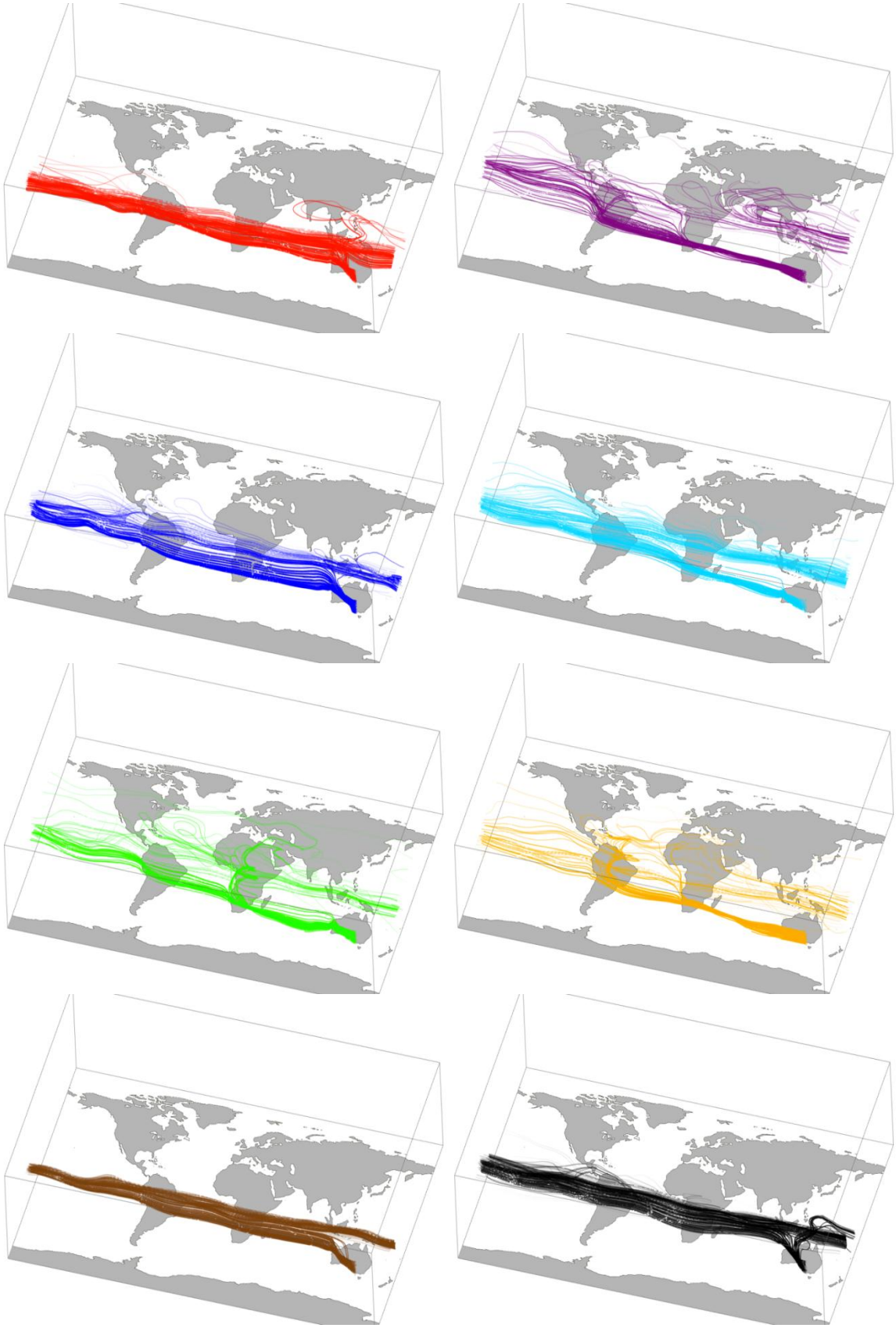

Figure 4-11. July 2001 Arrivals into Cape Grim with Three Months Lead Time

In Figure 4-11, July 2001 arrivals, the influence of the Southern Ocean is evident in all models, although this airstream has (typically) traveled north. Simulations P01, P03, P04, P07 and P08 show this airstream as the primary contributor to Tasmanian air with a few streams sweeping through southern Asia before final descent. Simulation P02 shows air entrainment from Africa and Asia, while simulations P05 and P06 incorporate air from a variety of Northern Hemisphere sources including Europe, the Atlantic and the North American jet stream. The primary Northern Hemisphere source for model P01 is southeast Asia. (Note the "epsilon" path taken over Africa near the equator in model P05.) We recall that the model simulations whose fossil fuel emission component most closely matched the phasing of the Cape Grim CO_2 cycle were P01 and P02 and that these were the only two to show residence in southeast Asia, a known major emitter of fossil fuel CO_2. Should either of these model runs be used alone for an inverse study regarding Tasmanian regional warming, potentially erroneous accusations might be made without further investigation.

Although January and July assessments are typically used to represent summer and winter processes or variable quantities respectively, CarbonTracker observations showed minimum CO_2 mixing ratios occur in May 2001 and maximum values in September 2001. Figures 4-12 and 4-13 illustrate flow paths into Cape Grim with three-month lead time for these months. For May 2001 arrivals, simulations show streamlines coming primarily from the Atlantic, Africa and southern Asia. P01, P02, P04 and P07 include paths taken through North America. Simulations P05-P08 include an Atlantic vortex into which Northern Hemisphere air is drawn to be delivered to the Southern Hemisphere. In September 2001, peak CO_2 values for the CarbonTracker data occur, while all of the GEOS-5 model simulations are in the middle of CO_2 decline here. Lowest CO_2 fossil fuel values occur in September 2001 for P08. This is also the only model for which the Southern Ocean air current is the only source of airstreams. Highest GEOS-5 model values during this month obtain for P01, P04, P05. The most varied paths to Cape Grim are taken by simulations P02, P03 and P07.

The Hadley circulation contributes to the interhemispheric transport through its seasonal oscillation (Bowman and Cohen, 1997). In response to seasonal solar heating, the Intertropical Convergence Zone (ITCZ) moves northward and southward (toward the warmer hemisphere), allowing air that was previously in one Hadley cell to be carried upward and poleward in the other Hadley cell. Additionally, transport within convective cells (such as those characteristic of tropical cyclones) increases the rate at which tracers are transported between adjacent convective rolls (Young et al., 1989). Therefore, it might be assumed that the CO_2 cycle at locations receiving Hadley cell air should be affected by surface sources in the other hemisphere.

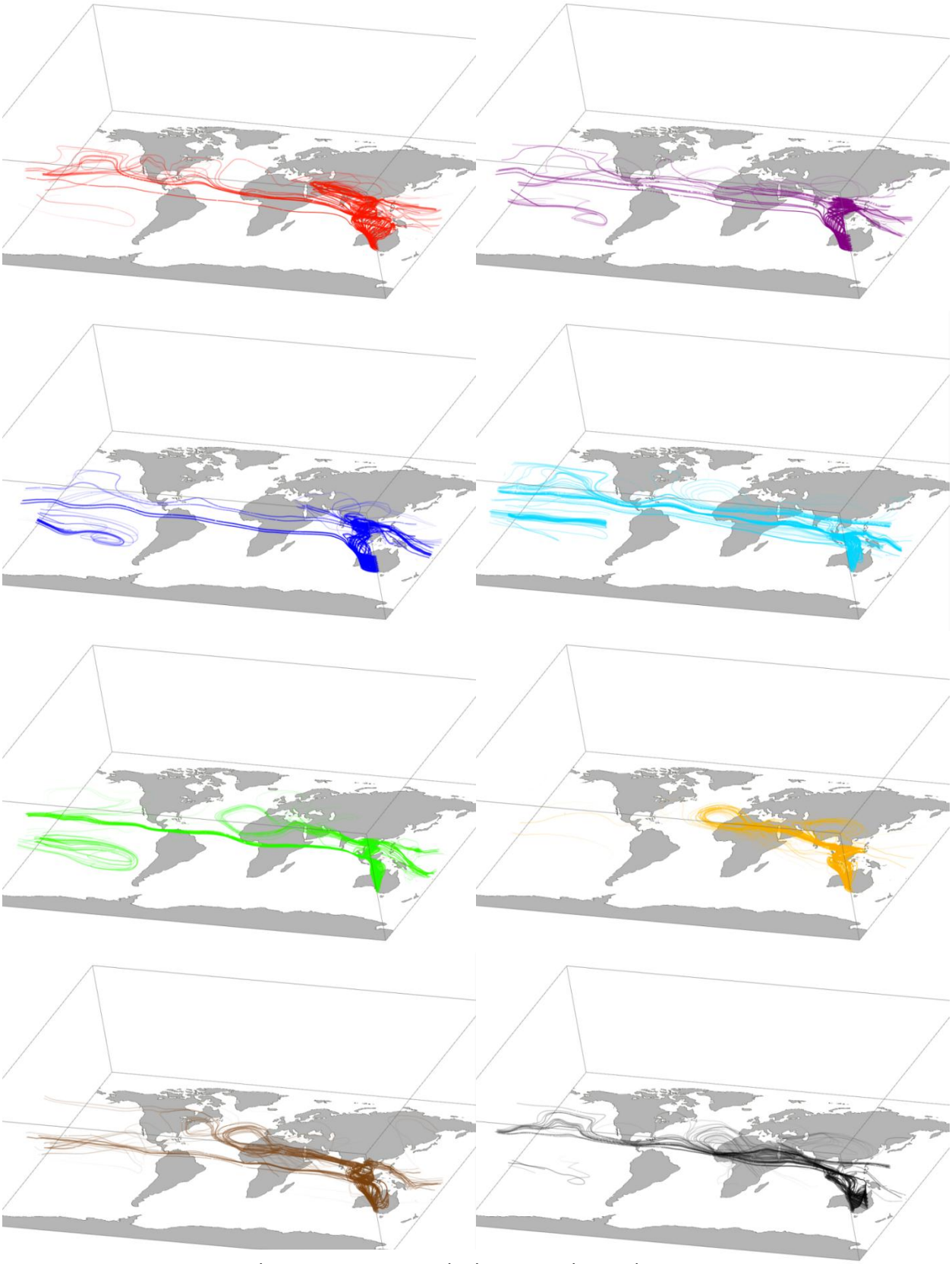

Figure 4-12. May 2001 Arrivals into Cape Grim with Three Months Lead Time

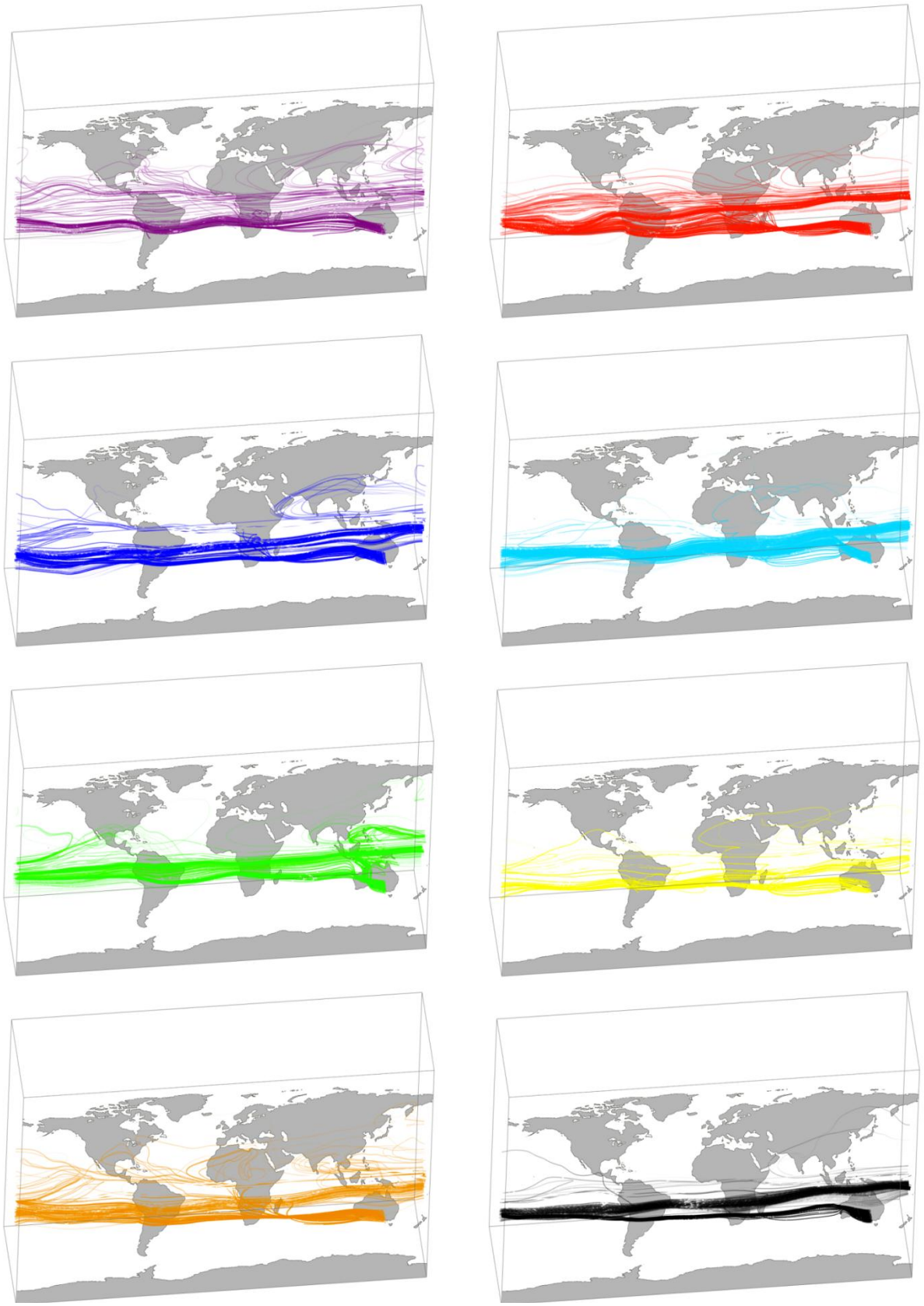

Figure 4-13. September 2001 Arrivals into Cape Grim with Three Months Lead Time

4.3.4 Comparison with Flow into Mauna Loa

Because it was assumed that varying routes of airflow affect the phasing of modeled CO_2 cycles at specific locations, we examine flow paths with three-month lead times into Mauna Loa for these months, since the simulations estimate well both amplitude and phasing at this location.

Figure 4-14 shows May 2001 arrival of air at Mauna Loa with 1 month lead time. All simulations indicate air parcels entering Mauna Loa from the Pacific vortex. Particles generally start in Eastern Canada or the North Atlantic and follow the jet stream to the Pacific. In P03-P08, Mid Atlantic air is drawn into Mauna Loa across North America. At three months in advance of May 2001 arrival, Figure 4-15 shows sources of air entering Mauna Loa include air from vortices located at 30S. These sources are swept into the equatorial current and then drawn into the Pacific vortex before entering Mauna Loa. Air particles that begin in the Southern Hemisphere follow a vertical pathway into the Northern Hemisphere.

In Figure 4-16, arrival Mauna Loa in September, 2001 with one month lead time is shown. Here it can be seen that as the ITCZ and the jet stream move south, the jet stream plays less a role in an airstream's previous month's travel into Mauna Loa than it does in May. Particles start in Canada and are pulled into the Pacific vortex across North America. All eight models follow similar paths. At three months in advance of arrival (Figure 4-17), southern sources of air undergo less activity in September than they do in May. Interhemispheric exchange occurs mainly in the region between eastern Africa and Indonesia. Northern paths originate in North America and the Atlantic Ocean. No Southern Hemisphere sources appear in P07. Few are included in P01.

In the case of the CO_2 cycle at Mauna Loa, all eight models are in phase with CarbonTracker and within a few ppm of the amplitude. In both May and September, all models follow similar one-month lead time paths to Mauna Loa. Northern Hemisphere sources (eastern Canada and the Atlantic Ocean) three months before arrival are similar for all models while Southern Hemisphere sources either vary or are not present. This suggests that Northern Hemisphere sources of air (and consequently, CO_2) have a larger effect on the amplitude and the phasing of the carbon cycle at Mauna Loa than Southern Hemisphere sources do. Likewise, varying initial meteorological conditions and consequent varying development of these conditions affect CO_2 concentrations less at Mauna Loa than they do at Cape Grim.

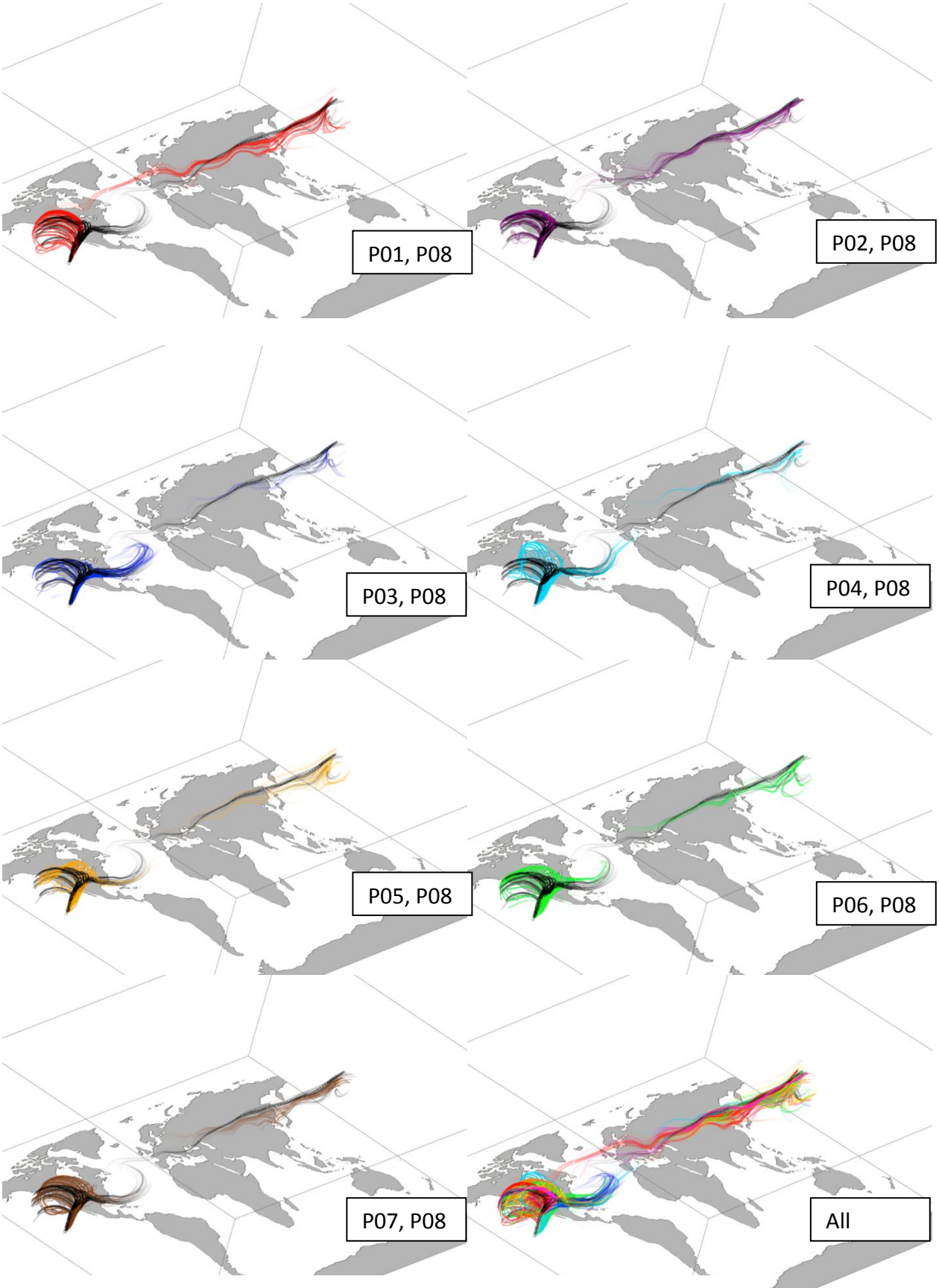

Figure 4-14. May 2001 Arrivals into Mauna Loa with One Month Lead Time

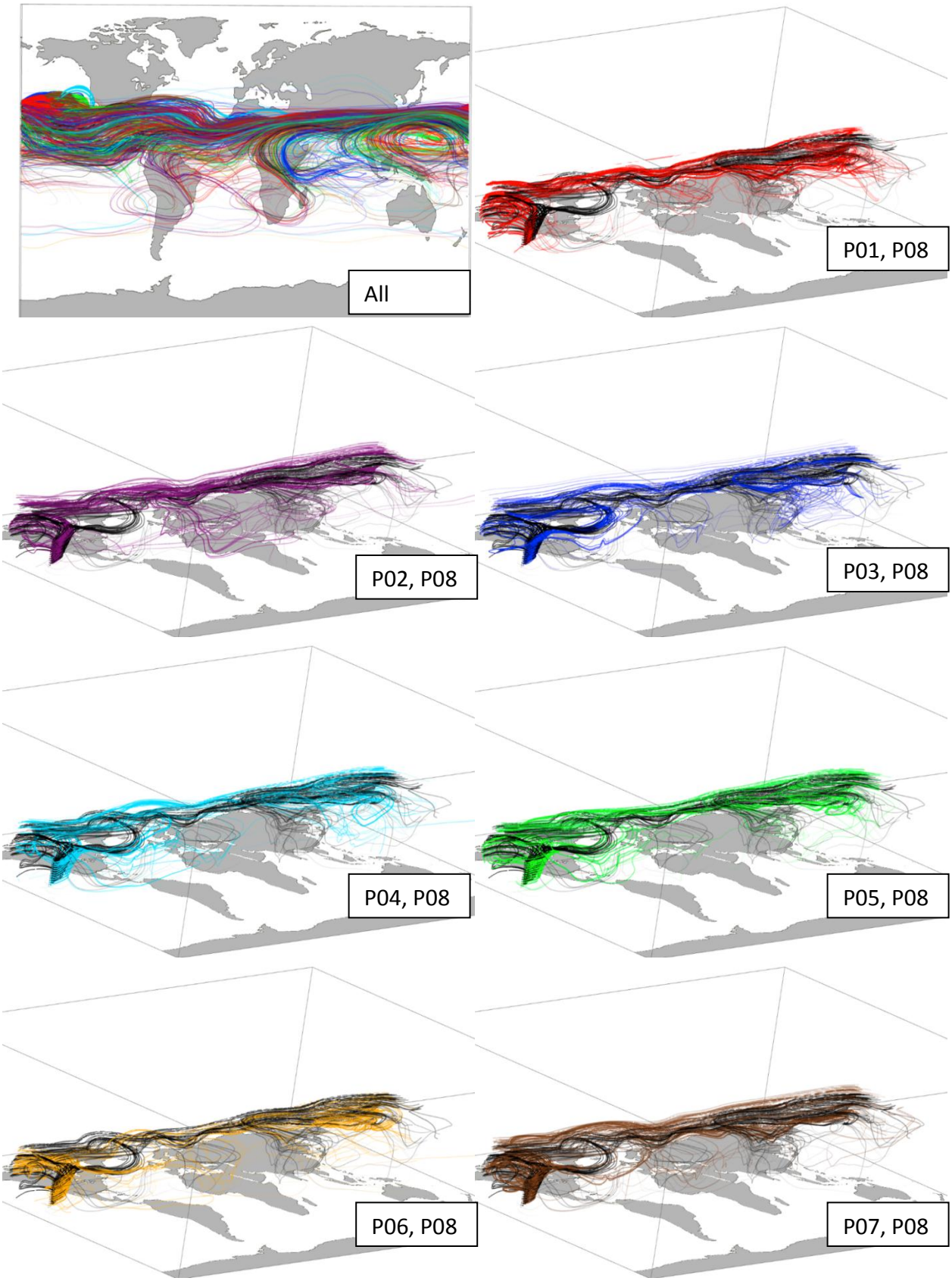

Figure 4-15. May 2001 Arrivals into Mauna Loa with Three Months Lead Time

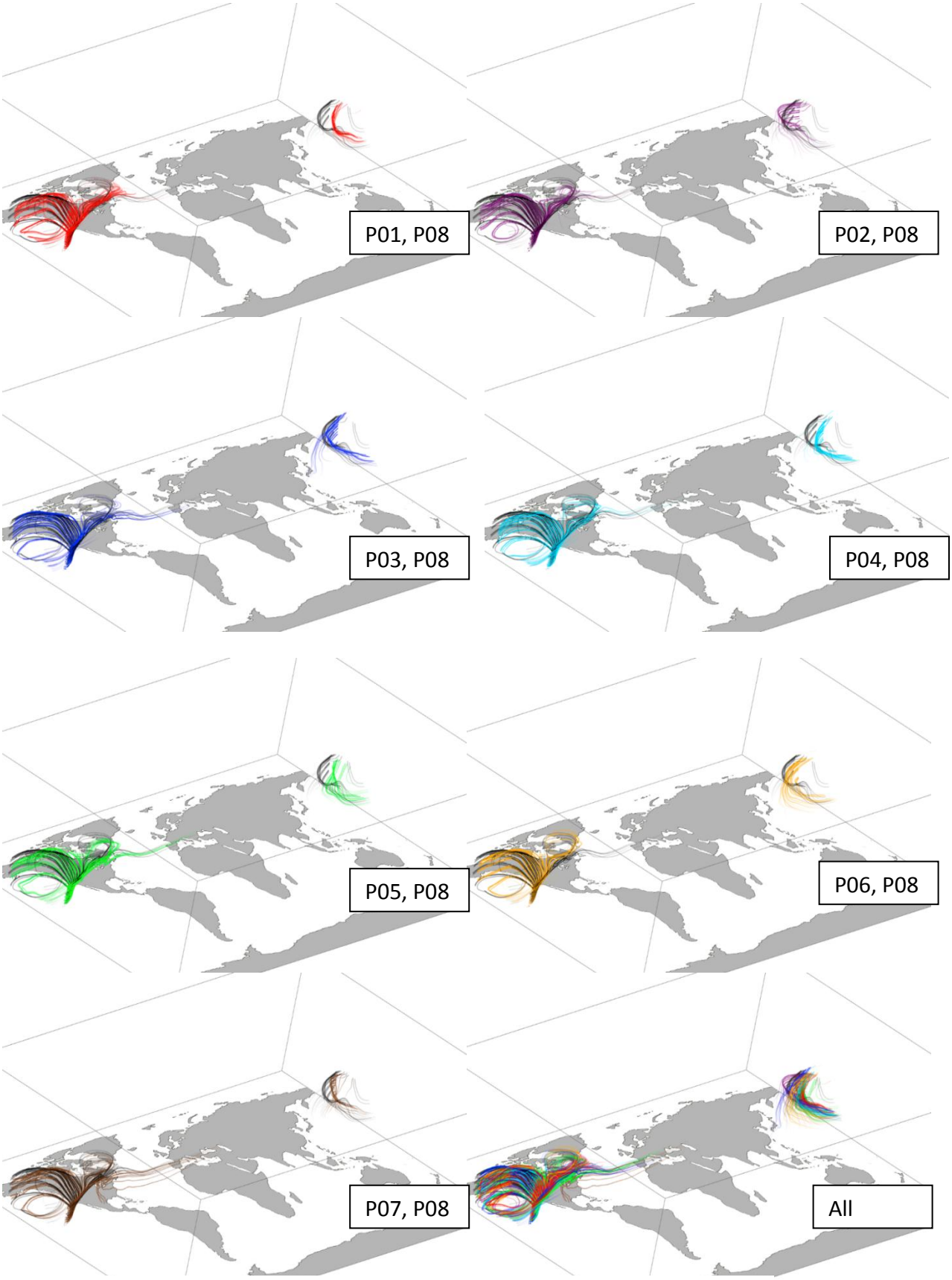

Figure 4-16. September 2001 Arrivals into Mauna Loa with One Month Lead Time

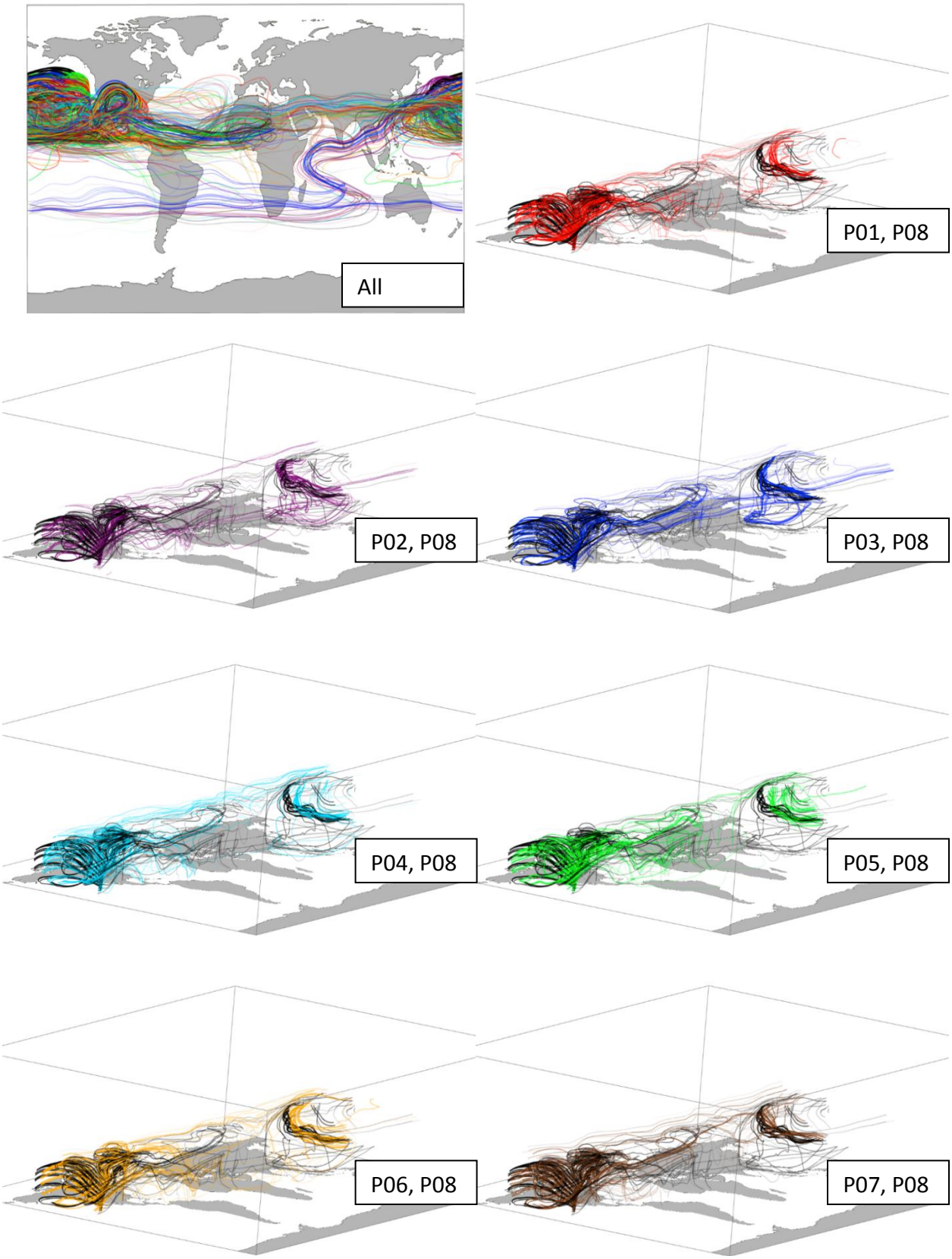

Figure 4-17. September 2001 Arrivals into Mauna Loa with Three Months Lead Time

4.4.0 Conclusions

In regions of high CO_2 emissions due to fossil fuel burning, large differences among the simulations appear for both the first month and the last month of the ensemble simulation. Thus in two years, individual simulations of an eight-member ensemble do not stabilize within a period of two years.

The phasing and amplitude of the CO_2 cycle at Northern Hemisphere locations in all of the ensemble members is similar to that of the CarbonTracker reanalysis, but in the southern hemisphere, GEOS-5 model cycles are out of phase by as much as four months, and large variations occur between the ensemble members. The most extreme differences occur among the ensemble and reanalysis data in the Cape Grim region with regard to CO_2 uptake and respiration of the terrestrial biosphere and CO2 emissions due to anthropogenic fossil fuel burning. While the amplitude of the cycle of the ocean and the terrestrial biosphere represent the largest percentages of the total CO_2 cycle, the phasing of fossil fuel CO_2 at 30-40% of the amplitude most closely follows the phase of the CO_2 total.

These findings suggest that although interhemispheric transport of CO_2 from fossil fuel produced in the Northern Hemisphere to the Southern Hemisphere may affect the phase of the CO_2 cycle in the Southern Hemisphere, internal model variability still obstructs the true fossil fuel CO_2 signal at specific sites in the Southern Hemisphere. Potential explanations for these discrepancies may lie in the robustness of the terrestrial biosphere flux data, model tuning or parameterization for the Southern Hemisphere; or in that higher concentrations of CO_2 in the Northern Hemisphere affect amplitude and phasing in the Southern Hemisphere more than circulation affects it in any location. We conclude that for inverse modeling of CO_2 and other species in the Southern Hemisphere, the effect of initial conditions on internal model variability is significant.

Acknowledgments. We acknowledge support from the NASA Carbon Cycle Science and the NASA High-End Computing Program. This research used resources of the National Center for Computational Sciences at Oak Ridge National Laboratory (ORNL).

CHAPTER V: SUMMARY AND CONCLUDING REMARKS

The National Aeronautics and Space Administration Goddard Earth Observation System model, Version 5 (GEOS-5) represents a state of the art climate model capable of simulating a wide variety of atmospheric processes informed continuously by satellite observations. Two aspects of the physical parameterizations employed by GEOS-5 and their effect on the transport of two greenhouse gasses: ozone and carbon dioxide, were examined in this paper.

For the first, which was a look at the impact on ozone (O_3) distribution and transport by varying the efficiency coefficients in the background and orographic gravity wave drag parameterizations in GEOS-5, a ten-member ensemble of simulations was generated. Each ensemble member contained a gravity wave drag treatment with different efficiency coefficients. Results from the simulations were compared to satellite observations and to National Oceanic and Atmospheric Association NCEP reanalyses of observations. No one simulation's gravity wave drag treatment proved most accurate in every comparison. Some simulations approximated variable quantities best in winter, others best in certain latitudes and still others best at higher altitudes. It was determined that measures for varying background gravity wave source, orographic factors and other tunable coefficients of gravity wave parameterization in order to more accurately capture seasonal, regional and vertical ozone distribution and transport, should be employed.

Meteorological development in eight different GEOS-5 model simulations given differing initial conditions was investigated in the second. With these simulations, internal model variability and its contribution to differences in interhemispheric transport of carbon dioxide (CO_2) were examined. The simulations incorporated CO2 flux data from four different sources/sinks: terrestrial biosphere, ocean, biomass burning and fossil fuel emissions. It was found that in the Northern Hemisphere, on a monthly temporal scale, differing initial conditions have little effect on model CO_2 cycles over the course of two years. In the Southern Hemisphere, however, because of complications in the development of terrestrial biosphere sources and sinks, fossil fuel flux sources, and in the phase shift extant in the ocean cycle; CO2 cycles in each of the simulations produced different cycle phasing and amplitudes. Likewise, each simulation produced different atmospheric flow paths into various specific regions. Thus it was determined, that for inverse modeling of CO_2 and other species in the Southern Hemisphere, the effect of initial conditions on internal model variability is significant.

Earth's atmosphere is a chaotic system, some aspects of which global models have come to represent well, and others which must continue to benefit from refinement. These two studies involving the GEOS-5 global circulation model, reveal minor weaknesses in the model whose modification can lead to more accurate predictions from the model, and ultimately, greater atmospheric insight.

COMPLETE LIST OF REFERENCES

American Meteorological Society Glossary. http://amsglossary.allenpress.com

Andres, R.J., G. Marland, I. Fung, E. Matthews (1996). A 1° x 1° distribution of carbon dioxide emissions from fossil fuel consumption and cement manufacture, 1950–1990, *Global Biogeochem. Cycles*. **10**, 419–429.

Beres, J. H., R. R. Garcia, B. A. Boville, and F. Sassi (2005). Implementation of a gravity wave source spectrum parameterization dependent on the properties of convection in the Whole Atmosphere Community Climate Model (WACCM), *J. Geophys. Res.*, **110**, D10108, doi:10.1029/2004JD005504.

Bloom, S., L. Takacs, A. DaSilva, and D. Ledvina (1996). Data assimilation using incremental analysis updates. *Mon. Wea. Rev.*, **124**, 1256-1271.

Bowman, K.P., and P.J. Cohen (1997). Interhemispheric Exchange by Seasonal Modulation of the Hadley Circulation. *Journal of the Atmospheric Sciences*, **54**, 2045-2059.

CarbonTracker 2010, http://carbontracker.noaa.gov

Chou, M.-D. and M.J. Suarez (1999). A Solar Radiation Parameterization for Atmospheric Studies. NASA *Technical Report Series on Global Modeling and Data Assimilation 104606*, **v15**, 40pp.

Chou, M.-D., M.J. Suarez, X.Z. Liang, and M.M.-H. Yan (2001). A Thermal Infrared Radiation Parameterization for Atmospheric Studies. NASA *Technical Report Series on Global Modeling and Data Assimilation 104606*, **v19**, 56pp.

Cordero, E., P.A. Newman, C. Weaver, and E. Flemming (2003). Stratospheric Ozone, *Studying Earth's Environment from Space.* NASA GSFC, Scientific and Educational Endeavors. http://www.ccpo.odu.edu/~lizsmith/SEES/ozone/oz_class.htm.

Denning, A.S., P.J. Rayner, R.M. Law, and K.R. Gurney (1998). Atmospheric Tracer Transport Model Intercomparison Project (TransCom). *IGBP/GAIM Report Series*, Report #4.

Denning, A. S., et al. (1999), Three-dimensional transport and concentration of SF6—A model intercomparison study (TransCom 2), Tellus, Ser.B, 51, 266–297.

Earth System Modeling Framework (ESMF). http://www.earthsystemmodeling.org/about_us

Erickson, D. J., III, R. T. Mills, J. Gregg, T. J. Blasing, F. M. Hoffman, R. J. Andres, M. Devries, Z. Zhu, and S. R. Kawa (2008). An estimate of monthly global emissions of anthropogenic CO2: Impact on the seasonal cycle of atmospheric CO2, *J. Geophys. Res.*, **113**, G01023, doi:10.1029/2007JG000435.
Erickson, D.J., R.J. Andres, M.S. Long, F.M. Hoffman, M.L. Branstetter, M.R. Allen (2011). Monthly fossil fuel CO_2 fluxes: Impact on atmospheric CO_2 seasonal cycles and implications for models of the terrestrial biosphere, Submitted to *Science*, June, 2011.

Fan, S. *et al*. A large terrestrial carbon sink in North America implied by atmospheric and oceanic carbon dioxide data and models. *Science*. ***282***, 442–446 (1998).

Froidevaux, L., et al. (2008). Validation of Aura Microwave Limb Sounder stratospheric ozone measurements, *J. Geophys. Res.*, **113**, D15S20, doi:10.1029/2007JD008771.

Garcia, R.R., S. Solomon (1985). The Effect of Breaking Gravity Waves on the Dynamics and Chemical Composition of the Mesosphere and Lower Thermosphere. *J. Geophys. Res.*, **90**(D2), 3850-3868.

Garcia, R.R., F. Stordal, S. Solomon, J.T. Kiehl (1992). A New Numerical Model of the Middle Atmosphere 1. Dynamics and Transport of Tropospheric Source Gases. *J. Geophys. Res.*, **97**(D12), 12,967-12,991.

Garcia, R.R., and B.A. Boville (1994). "Downward Control" of the Mean Meridional Circulation and Temperature Distribution of the Polar Winter Stratosphere. *J. Atmos. Sci.*, **51**, 2238–2245.

Gurney, K. R., L. M. Rachel, A. S. Denning, P. J. Rayner, D. Baker, P. Bousquet, L. Bruhwiler, Y.-H. Chen, P. Ciais, S. Fan, I. Y. Fung, M. Gloor, M. Heimann, K. Higuchi, J. John, T. Maki, S. Maksyutov, K. Masarie, P. Peylin, M. Prather, B. C. Pak, J. Randerson, J. Sarmiento, S. Taguchi, T. Takahashi, and C.-W. Yuen. (2002). Towards robust regional estimates of CO2 sources and sinks using atmospheric transport models. *Nature*, **415**, 626–630.

Gurney, K.R., *et al*. (2005). Sensitivity of atmospheric CO2 inversions to seasonal and interannual variations in fossil fuel emissions. *J. Geophys. Res*. **110***,* (D10) D10308.

Hansen, J.E. (2002). Workshop background. In *Air Pollution as a Climate Forcing: Proceedings of a Workshop* (J.E. Hansen, Ed.). NASA Goddard Institute for Space Studies. New York.

Heimann, M., and C. D. Keeling (1986). Meridional eddy diffusion model of the transport of atmospheric carbon dioxide. Part 1, Seasonal carbon cycle over the tropical Pacific Ocean. *J. Geophys. Res.,* **91,** 7765–7781.

Holton, J.R, P.H. Haynes, M.E. McIntyre, A.R. Douglass, R. Rood, L. Pfister (1995). Stratosphere-Troposphere Exchange, *Reviews of Geophysics*, **33**, 4, Paper number 95RG02097, American Geophysical Union.

Holton, J.R (2004). *An Introduction to Dynamic Meteorology*, Elsevier, San Diego, 535pp.

Japan Meteorological Agency: Model JMA GSM (TL959 L60) 20031216-MRICLIM (2003). http://www.jamstec.go.jp/kakushin21/kyousei/k041open/data/modeldoc.html

Kawa, S. R., D. J. Erickson III, S. Pawson, and Z. Zhu (2004). Global CO2 transport simulations using meteorological data from the NASA data assimilation system, *J. Geophys. Res.*, ***109***, D18312.doi:10.1029/2004JD004554.

Keeling, C.D., R.B. Bacastow, A.E. Bainbridge, C.A. Ekdahl, P.R. Guenther, and L.S. Waterman (1976). Atmospheric carbon dioxide variations at Mauna Loa Observatory, Hawaii, *Tellus*, **28**, 538-551.

Kendall, W., J. Wang, M. Allen, T. Peterka, J. Huang, and D. Erickson (2011). Simplified Parallel Domain Traversal. *SC `11: Proceedings of ACM/IEEE Supercomputing*.

Kepert, J. (2009). 4D Var for Dummies. Presentation for Centre for Australian Weather and Climate Research, A partnership between the Australian Bureau of Meteorology and CSIRO, 8th Adjoint Workshop, Pennsylvania, May 17-22.

Kiehl J.T., J. Hack, G. Bonan, B. Boville, B. Briegleb, D. Williamson, and P.J. Rasch (1996). *Description of the NCAR Community ClimateModel (CCM3).* Technical Report NCAR/TN-420+STR, National Center for Atmospheric Research, Boulder, Colorado.

Kiehl, J. T., T. L. Schneider, R. W. Portmann, and S. Solomon (1999). Climate forcing due to tropospheric and stratospheric ozone, *J. Geophys. Res.*, 104(D24), 31,239–31,254, doi:10.1029/1999JD900991.

Lait, L. R., M. R. Schoeberl, and P. A. Newman, 1989: Quasi-biennial modulation of the Antarctic ozone depletion. *J. Geophys. Res.,* **94,** 11 559–11 571.

Lamarque, J.-F., A.O. Langford, M.H. Proffitt (1996). Cross Tropopause Mixing of Ozone Through Gravity Wave Breaking: Observation and Modelling, *J. Geophys. Res.*, **101**(D17), 22969, 1996.

Law, R. M., Rayner, P. J., Denning, A. S., Erickson, D., Heimann, M., Piper, S. C., Ramonet, M., Taguchi, S., Taylor, J. A., Trudinger, C. M., and Watterson, I. G. (1996). Variations in modelled atmospheric transport of carbon dioxide and the consequences for CO2 inversions, *Global Biogeochemical Cycles*, **10**, 783-796.

Lin, Shian-Jiann (2004). A "Vertically Lagrangian" Finite-Volume Dynamical Core for Global Models. *Monthly Weather Review*, **132**, 2293-2307.

Lindzen, R. S. (1981). Turbulence and Stress Owing to Gravity Wave and Tidal Breakdown, *J. Geophys. Res.*, **86**(C10), 9707–9714.

Livesey, Nathaniel J., et al. (2007). *Version 2.2 Level 2 data quality and description document*. JPL D-33509, Jet Propulsion Laboratory, Californa Institute of Technology, Pasadena, CA, 91109-8099.

Livesey, N. J., et al. (2008). Validation of Aura Microwave Limb Sounder O_3 and CO observations in the upper troposphere and lower stratosphere, *J. Geophys. Res.*, **113**, D15S02, doi:10.1029/2007JD008805.
McFarlane, N., (1987). The Effect of Orographically Excited Gravity Wave Drag on the General Circulation of the Lower Stratosphere and Troposphere. *J. Atmos. Sci.*, **44**, 1775–1800.
Lock, A.P., A.R. Brown, M.R. Bush, G.M. Martin, and R.N.B. Smith (2000). A new boundary layer mixing scheme. Part I: Scheme description and single-column model tests. *Mon. Wea. Rev.*, **138**, 3187-3199.

Louis, J., M. Tiedtke, and J. Geleyn (1982). A short history of the PBL parameterization at ECMWF. *Proc. ECMWF Workshop on Planetary Boundary Layer Parameterization,* Reading, United Kingdom, ECMWF, 59–80.

Marshall, G. J. (2003). Trends in the Southern Annular Mode from observations and reanalyses, *J. Climate*, **16**, 4134-4143.

Marshall, J. and R.A. Plumb (2008). *Atmosphere, Ocean and Climate Dynamics: An Introductory Text,* Massachussetts Institute of Technology, Cambridge, 319pp.

Moorthi, S., and M.J. Suarez (1992). Relaxed Arakawa-Schubert, A Parameterization of Moist Convection for General-Circulation Models. *Mon. Wea. Rev.* **120**, 978-1002.

Ollers, M.C., L. P. J. Kamp, F. Lott, P. F. J. Van Velthoven, H. M. Kelder, And F. W. Sluijter (2003). Propagation properties of inertia–gravity waves through a barotropic shear layer and application to the Antarctic polar vortex, *Q. J. R. Meteorol. Soc.* (2003), **129**, pp. 2495–2511.

Ott, L.E., J. Bacmeister, S. Pawson, K. Pickering, G. Stenchikov, M. Suarez, H. Huntrieser, M. Loewenstein, J. Lopez, and I. Xueref-Remy (2009). Analysis of Convective Transport and Parameter Sensitivity in a Single Column Version of the Goddard Earth Observation System, Version 5, General Circulation Model, *Journal of the Atmospheric Sciences*, **66**, 627-646.

Plumb, R.A. (2002). Stratospheric transport, *J. Met. Soc. Japan* , **80**, 793-809.

Pawson, S., R.S. Stolarski, A.R. Douglass, P.A. Newman, J.E. Nielsen, S.M. Frith, and M.L. Gupta (2008). Goddard Earth Observing System chemistry-climate model simulations of statospheric ozone-temperature coupling between 1950 and 2005, *J. Geophys. Res.,* **113**, D12103, doi:10.1029/2007JD009511.

Peters et al., (2007). An atmospheric perspective on North American carbon dioxide exchange: CarbonTracker, *PNAS,* **104***/*48, 18925-18930.

Randerson, J.T., M.V. Thompson, T.J. Conway, I.Y. Fung, and C.B. Field (1997). The contribution of terrestrial sources and sinks to trends in the seasonal cycle of atmospheric carbon dioxide. *Global Biogeochemical Cycles*, **11**, 535-560.

Randerson, J. T., G. R. van der Werf, L. Giglio, G. J. Collatz, and P. S. Kasibhatla, Global Fire Emissions Database, Version 2 (GFEDv2.1), Data set, Available from Oak Ridge National Laboratory: http://daac.ornl.gov/

Rienecker, M.M, M.J. Suarez, R. Todling, J. Bacmeister, L. Takacs, H.-C. Liu, W. Gu, M. Sienkiewicz, R.D. Koster, R. Gelaro, I. Stajner, and J.E. Nielsen (2008). The GEOS-5 Data Assimilation System—Documentation of Versions 5.0.1, 5.1.0, and 5.2.0, *Technical Report Series on Global Modeling and Data Assimilation*, **27**, NASA/TM–2008–104606.

Stolarski, R.S., A.R. Douglass, M. Gupta, P.A. Newman, S. Pawson, M.R. Schoeberl, and J.E. Nielsen (2006). An ozone incresase in the Antarctic summer stratosphere: A dynamical response to the ozone hole, *Geophysical Research Letters* , **33**, L21805, doi:10.1029/2006GL026820.

Takahashi, T., Wanninkhof, R.H., Feely, R.A., Weiss, R.F.,Chipman, D.W., Bates, N., Olafsson, J., Sabine, C., Sutherland, S.C. (1999). Net sea–air CO_2 flux over theglobal oceans: An improved estimate based on the sea–air pCO_2 difference. In: Yukihiro Nojiri (Ed.), Proceedings of the Second International Symposium, CO_2 in the Oceans (ISSN 1341-4356), Center for Global Environmental Research, National Institute for Environmental Studies, Tsukuba, Japan, pp. 9–14.

Teitelbaum, H., J. Ovarlez, H. Kelder, and F. Lott (1994), Some observations of gravity-wave-induced structure in ozone and water vapour during EASOE, *Geophys. Res. Lett.*, **21**(13), 1483–1486.

Thompson, D.W.J., S. Solomon (2002), Interpretation of Recent Southern Hemisphere Climate Change, *Science* **296**, 895 (2002); DOI: 10.1126/science.1069270.

Van der Werf, G. R., J. T. Randerson, L.Giglio, G. J. Collatz, and P. S. Kasibhatla (2006). Interannual variability in global biomass burning emission from 1997 to 2004, *Atmospheric Chemistry and Physics*, **6**, 3423-3441.

Vial, F., Babiano, A., Brioit, B., Basdevant, C., Legras, B., Sadourny, R., Ovarlez, H., et al. (1995). Stratéole: A project to study antarctic polar vortex dynamics and its impact on ozone chemistry. *Physics and Chemistry of the Earth*, ***20***(1), 83-96.

Young, W., A. Pumir, and Y. Pomeau (1989). Anomalous diffusion of tracer in convection rolls. *Phys. Fluids A,* **1,** 462–469.

APPENDIX

APPENDIX: A SIMPLIFIED EXPRESSION OF THE OROGRAPHIC WAVE DRAG MODEL (MCFARLANE, 1987)

Although the full gravity wave drag parameterizations are described in more detail in the above-mentioned papers, the fundamental equation for the wave drag force incorporated within the GEOS-5 hybrid sigma pressure coordinate system can be expressed:

$$(\partial \vec{V}/\partial t)g = -\vec{n}\partial(MU)/\partial\sigma$$

where U = local airflow, n is a unit vector parallel to the reference level flow and g is gravitational acceleration. M is defined:

$$M = \propto \sigma N A^2/H$$

Here, H = local density scale height, A = the wave amplitude, and $\alpha = E\mu/2 = 8 \times 10^{-6}\ m^{-1}$ with μ = the horizontal wavenumber and E = an efficiency factor which is less than 1. (In this simulation, the efficiency factor E is set to the value of 0.125 in accordance with WACCM1b (Kiehl et al. 1996), on which the parameterizations are based.) σ is the pressure coordinate = p/p_s with p_s equal to surface pressure.

N = the Brunt-Vaisala frequency at the mean potential temperature, is of the form:

$$N^2 = \frac{g}{\bar{\theta}}\frac{\partial\bar{\theta}}{\partial z}$$

and is always a positive real value. The potential temperature, θ, is expressed in units of Kelvin.

In wave saturation regions, A is chosen such that the quantity $AN/F_c U = 1$ so that in those regions,

$$M = \propto \sigma {F_c}^2 U^2/(NH)$$

with Fc representing the local Froude number. The value of Fc^2 in the parameterization is set to the default of 0.5.

VITA

Melissa Ree McGuire Allen was born in Longmont, Colorado to Daniel and Patricia McGuire, and was pleased two years later to welcome her younger sister, Holly, to her world. She graduated from Longmont High School in the spring of 1984; and in the fall of the same year, entered the University of Northern Colorado as violin student of Professor Richard Fuchs and a Ginsburg String Scholarship awardee Music Education major. She graduated with honors in the spring of 1989, receiving in 1988 the UNC School of Music Departmental Scholar Award for Academic Excellence.

For two years after graduation, she taught orchestra and choir at the middle and high school levels in Greeley, Colorado, and complemented her teaching with professional violin playing in both Colorado and Wyoming orchestras. Then she moved to Albuquerque, New Mexico to become Office Manager, Sales and Shipping coordinator for the nationally and internationally renowned Robertson and Sons Violin Shop.

In 1996, she married her husband, John Allen of Knoxville, Tennessee and relocated with him to East Tennessee. From 1996-2011, she taught private violin and viola lessons to students in the Maryville City Schools orchestra program. Also in 1996, inspired by a flight in a Waco biplane that she shared with her husband on their honeymoon in Kittyhawk, North Carolina, she began flying single-engine airplanes at the Knoxville Downtown Island Airport. With instruction from John McConkey through the Knoxville Flight Training Center, she earned her Private Pilot Certificate in 1997 and the Instrument Rating in 1998. It was during this process that she became intrigued with weather, climate and earth's atmosphere.

During the years 2001-2004, Ms. Allen completed core calculus and linear and vector algebra courses through the University of Illinois, Champaign. As she began to prepare for a future in climate research, she subsequently completed a year of General Chemistry and a year of calculus-based Physics at Pellissippi State Technical Community College. She began a research assistantship at Oak Ridge National Laboratory in the Computational Earth Sciences group with Dr. David Erickson in 2008 during which she gained experience with global climate models (NASA and NCAR) and simulations using the Jaguar, Kraken and Lens supercomputers, and with a variety of analysis tools and visualization software.

She entered the University of Tennessee in the fall of 2009 as a student of Dr. Joshua Fu in Environmental Engineering with a concentration in Climate Studies. Through collaboration among University departments and with Oak Ridge National Laboratory, she has been involved in a variety of projects leading to abstracts, publications and presentations for organizations such as the American Geophysicists Union, Supercomputing, IEEE, Oak Ridge National Laboratory and interested community groups.

Upon August 2011 graduation, Melissa Allen will enter the Energy Science and Engineering Department as an ESE fellow within the University of Tennessee Center for Interdisciplinary Research and Graduate Education Program to pursue the Doctor of Philosophy Degree. Her dissertation will focus on the effects of climate change on energy production. Along with a healthy appetite for scientific modeling and discovery of atmospheric, environmental and energy processes, Melissa Allen also retains a palate for string chamber music playing, aviation and mountain hiking with friends both human and canine. She aspires to a life that includes opportunities for enjoyment and productivity in all.